



RESEARCH ARTICLE

10.1029/2023JD039180

XStorm: A New Gamma Ray Spectrometer for Detection of Close Proximity Gamma Ray Glows and TGFs

Melody Pallu^{1,2,3,4} , Sebastien Celestin¹ , Yanis Hazem¹ , François Tromprier³ , and Gaël Patton⁵

¹LPC2E, CNRS, University of Orleans, Orleans, France, ²Institute of Radiation Protection and Nuclear Safety (IRSN), Fontenay-aux-Roses, France, ³Occupational Health Services, Air France, Roissy-en-France, France, ⁴Now at Université Paris Cité, CNRS, CNES, Astroparticule et Cosmologie, Paris, France, ⁵Icohub, Limoges, France

Key Points:

- Development of a gamma ray spectrometer to detect gamma ray glows and terrestrial gamma ray flashes (TGFs), able to discriminate photons, electrons, and neutrons
- Results from balloon test flights performed in fair weather conditions, detecting the background radiation level as a function of altitude
- Estimation of the detectability of gamma ray glows and TGFs as a function of altitude with XStorm

Correspondence to:

S. Celestin,
sebastien.celestin@cnrs-orleans.fr

Citation:

Pallu, M., Celestin, S., Hazem, Y., Tromprier, F., & Patton, G. (2023). XStorm: A new gamma ray spectrometer for detection of close proximity gamma ray glows and TGFs. *Journal of Geophysical Research: Atmospheres*, 128, e2023JD039180. <https://doi.org/10.1029/2023JD039180>

Received 28 APR 2023
Accepted 30 NOV 2023

Abstract In this paper, we present XStorm, a gamma ray spectrometer developed to detect gamma ray glows and terrestrial gamma ray flashes (TGFs) in close proximity. Measurements are mostly planned to take place on balloon campaigns but also on the ground using bigger detectors. The main aim in developing XStorm is to perform new in situ and close proximity measurements of those events to improve the understanding of the physical processes involved. For that, we ensured XStorm reached performances adapted to glow and TGF detections. It detects photons with energy between ~ 400 keV and ~ 20 MeV. Detected particles are timetagged with a 600 ns precision with respect to UTC. Using two types of scintillator, Bismuth Germanium Oxide and EJ-276 plastic associated with SiPMs, the instrument is able to discriminate three types of particles involved in those events: photons, neutrons, and electrons. The behavior of the detector under high particle fluxes has been quantified through ground testing using a pulse generator. A triggered detection system has been developed, with different thresholds depending on the target of study. First measurements have been carried out with test flights in fair weather conditions and are presented here. Estimations of the configurations in which a gamma ray glow can be detected by XStorm and of the number of TGFs that could be detected in specific campaigns are also addressed.

Plain Language Summary Terrestrial gamma ray flashes (TGFs) are bursts of high-energy photons generated in thunderstorms in less than 100 μ s, whereas gamma ray glows are enhancement of the high-energy radiation background in thunderstorms, lasting from seconds to minutes. We present a gamma ray spectrometer, XStorm, designed to detect terrestrial gamma ray flashes (TGFs) and gamma ray glows in close proximity. It is composed of two scintillators of different kinds to allow the detection of TGF and gamma ray glow photons (energies between 400 keV and 20 MeV, with a time precision of 600 ns UTC). XStorm measurements are mainly planned to take place on board balloons, but can also be performed at ground level using bigger scintillators. XStorm is able to discriminate photons, electrons and neutrons, that are particle types involved in TGFs. We show the first measurements in fair weather and configurations allowing the detection of gamma ray glows. We estimate that XStorm will detect ~ 0.5 TGF on average over one balloon flight of Stratéole-2 campaign presented in the scientific objectives.

1. Introduction

Terrestrial gamma ray flashes (TGFs) and gamma ray glows are two types of high-energy events produced in thunderstorms generating gamma rays (Fishman et al., 1994; Parks et al., 1981). They have different fluxes, and durations but can be driven by the same fundamental physical processes, namely runaway electron acceleration (e.g., Dwyer et al., 2012; Gurevich et al., 1992) and photon production through bremsstrahlung. Some gamma ray glows can be driven by the Modification Of Spectra (MOS) mechanism (e.g., Chilingarian et al., 2010). TGFs and gamma ray glows are both produced at thunderstorm altitudes, with a detection altitude ranging up to ~ 20 km for gamma ray glows (depending on intensity). In order to improve the understanding of these events, we identified the need to develop a lightweight gamma ray spectrometer able to detect high fluxes of particles. The use of sounding balloons allows to perform measurements close to the sources, bringing new information on the physical mechanisms at the origin of these events.

In Section 2, we expose the scientific objectives of XStorm (Figure 1), a new gamma ray spectrometer to detect gamma ray glows and TGFs in close proximity to be flown on balloon campaigns, presenting TGFs and gamma ray glows, as well as the measurement campaigns already planned for XStorm. In Section 3, we present an

© 2023. The Authors.

This is an open access article under the terms of the [Creative Commons Attribution License](#), which permits use, distribution and reproduction in any medium, provided the original work is properly cited.

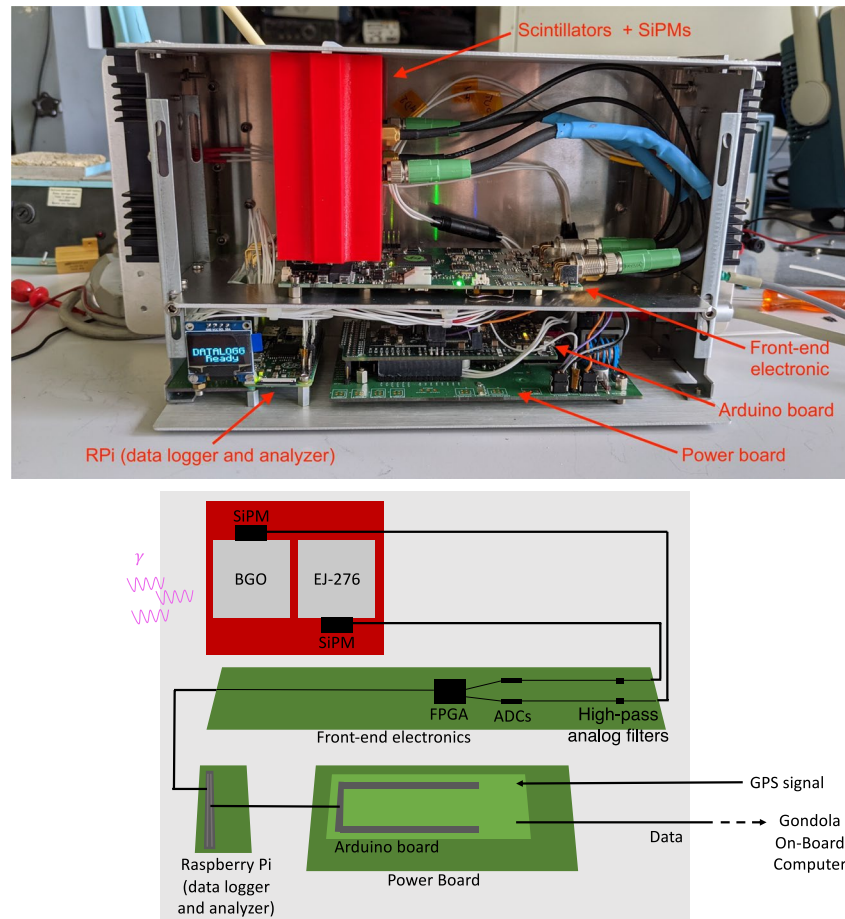


Figure 1. XStorm adapted for Strateole-2 campaigns (mechanical, communication, and power interfaces). The scintillators are coupled with SiPMs, and are contained in the red box. They are connected to the front-end electronics, which analyze the signal giving the following outputs: time arrival and energy of each particle detected. Those high-resolution data are sent to the Raspberry Pi to be recorded and/or sent (depending on the project) to the on-board computer of the balloon gondola through the Arduino board. If payload recovery is not possible for the project, data are sent through a satellite link to the ground.

overview of XStorm including the performances, the triggering processes, and the different data modes. The first measurements made in fair weather conditions are presented in Section 4. Finally, estimations to evaluate the future detections of gamma ray glows and TGFs are presented in Section 5.

2. Scientific Objectives

The main objectives of the gamma ray spectrometer are to detect high-energy atmospheric electric events such as gamma ray glows usually produced and detected inside thunderstorms, but also detected above thundercloud tops at high-altitude (20 km) as recently reported by Østgaard, Christian, et al. (2019), and TGFs, which are usually detected by satellites. In fact, the spectrometer is due for flying on balloons to perform in situ and close proximity measurements in thunderstorms to improve understanding of physical processes that are still uncertain as to how seeding and acceleration process are engaged, to quantify better the rarity of weak TGFs (i.e., not detectable by satellite), and refine reported results about radiation dose and exposure risks associated with TGFs (e.g., Dwyer et al., 2010; Pallu et al., 2021, 2023).

Secondary objectives are phenomena leading to an increase of high-energy radiation in the lower stratosphere, such as Solar Energetic Proton events (accelerated protons emitted by the Sun) and Gamma Ray Bursts (powerful cosmic explosions producing gamma rays, coming from distant galaxies). They are composed of gamma rays in the range of energy covered by XStorm, and are also transient events, hence the possibility to detect them.

2.1. Gamma Ray Glows

Gamma ray glows are enhancements of the background radiation in thunderstorms. They can last from seconds to tens of minutes and are not bright enough to be detected far away (such as by satellite as TGFs) from the thunderstorm. They are believed to be produced either by relativistic runaway electron avalanches (RREAs) (e.g., Dwyer et al., 2012) and bremsstrahlung, or by the MOS mechanism (Chilingarian et al., 2010). The latter explains the presence of enhanced fluxes of gamma rays when the electric field strength is weaker than the RREA threshold, but sufficient to give enough energy to cosmic background electrons and positrons. As they are presumably more frequent than TGFs and as they last longer, they are the first objective constraining the design of this spectrometer (e.g., Kelley et al., 2015; Østgaard, Neubert, et al., 2019). The aims are to investigate runaway electron acceleration processes, study their link with cosmic rays, and determine their contribution to the general discharging mechanism of the storms (Kelley et al., 2015).

For instance, gamma ray glows have already been detected by several means of measurement. McCarthy and Parks (1985) and Parks et al. (1981) have presented among the first reports of such observations using an aircraft. Balloon measurements were performed by Eack et al. (1996) simultaneously with electric field measurements. 12 gamma ray glows have been detected by an airborne detector during the ADELE campaign, within 37 flight hours (Kelley et al., 2015). Ground-based measurements have been made in low altitude winter thunderstorm in Japan (e.g., Wada et al., 2019) followed by a downward TGF and measured by two different detectors. Other ground-based measurements at Mount Aragats high-altitude research station in Armenia (e.g., Chilingarian et al., 2019) have been performed. Studying gamma ray glows helps understand the physical processes involved in both gamma ray glows and TGFs. Gamma ray glows and TGFs can be detected at the same time (Smith et al., 2018; Wada et al., 2019). Recently, two gamma ray glows have been detected at high-altitude (20 km) (Østgaard, Christian, et al., 2019). These measurements introduce new questions concerning the general context in which gamma ray glows can be produced.

2.2. Terrestrial Gamma Ray Flashes

TGFs are bursts of photons produced in association with lightning discharges. TGFs detected from space have been particularly associated with positive intracloud (+IC) discharges (e.g., Cummer et al., 2011, 2015; Lu et al., 2011; Shao et al., 2010). They last ~ 100 μ s, produce photons up to 40 MeV energies, and are very bright. Their detection is mostly made by satellite. The same processes as glows drive their production: RREAs and bremsstrahlung (Kelley et al., 2015). Moreover, they can occur simultaneously with glows (e.g., Wada et al., 2019) and TGFs tend to occur in high-field regions (Cummer et al., 2015). Therefore it is interesting to study these events simultaneously. The aims in detecting TGFs with XStorm are to observe these events in close proximity, to quantify radiation doses in thunderstorms, because only estimations by calculation have been made until now (e.g., Pallu et al., 2021), assess their frequency of occurrence (Pallu et al., 2023), and to detect radionuclide and neutron signatures (e.g., Bowers et al., 2017; Enoto et al., 2017; Rutjes et al., 2017). Ground-based measurements are now quite frequent as well, especially thanks to the Telescope Array that is continuously able to detect downward TGFs (Abbasi et al., 2017, 2018; Belz et al., 2020). However, airborne measurements of TGFs have been performed only twice (Bowers et al., 2018; Smith et al., 2011), and TGF detections with the gamma ray spectrometer presented in this paper during a balloon campaign is likely to add new information on the characteristics of the sources.

2.3. Measurement Campaigns

To answer these questions, XStorm detectors will fly on balloon campaigns and be installed on high-altitude ground-based locations within the framework of several projects.

The first project, funded by the French Space Agency (CNES) is called Observation du Rayonnement Énergétique dans les Orages (OREO). The aim of this project is to launch clusters of weather balloons into thunderstorms, going from ground to ~ 30 km and back, in ~ 2 – 3 hr. Clusters of 3–4 balloons will be launched. Each gondola will be equipped with XStorm and an electric field mill to measure the local electrostatic field. The constraints on XStorm for this campaign is mainly the weight (< 3 kg), as all the data will be stored on-board, payloads being recovered at the end of the flights. The objectives of this project is to make close and multipoint measurements of gamma ray glows and TGFs. First campaigns will take place in France, in 2024.

The second project is called Stratéole-2. It is a French-US project funded by CNES and the U.S. National Science Foundation. It consists in several stratospheric balloon campaigns with long duration (~2–3 months) superpressure balloons flying between 18 and 20 km altitude in the intertropical region. The objectives of the scientific campaigns are to study exchanges between the high troposphere and the low stratosphere at low latitudes. Two previous campaigns have been organized in 2019 and 2021, the next one is planned in 2025. These flight characteristics are ideal for our main scientific targets, because four copies of XStorm are planned to fly for long durations above thunderstorm altitudes, and in most active region in terms of thunderstorm occurrence. STRatéole-2 ATmospheric ELEctricity (STRATELEC) is a connected project, which is also funded by CNES and aims to develop an instrumental payload dedicated to the study of atmospheric electricity to be flown during Stratéole-2 next scientific campaign.

On Stratéole-2 campaign, XStorm had to be constrained in weight, size, power, and telemetry (TM) demands. The weight is less constrained than on weather balloons, as the mass can be up to ~5 kg, depending on the other instruments of the gondola. But the no-recovery of the instruments calls for a precisely tailored TM strategy and a power and communication interfaces fitting the gondola and On-Board Computer (OBC) specifications. A triggering process has been developed in order to select interesting periods for which high resolution data are to be sent down to the ground. These features are developed in the next section.

On the ground, with less restrictive constraints concerning weight and size, bigger detectors will be used (typically 3"- to 5"-side scintillators) in the framework of an ongoing project with the French Institute of Radiation Protection and Nuclear Safety (IRSN). The absence of constraints on data storage will allow the detectors to record data during several months, from the summer 2023. The locations will be chosen to ease the detection of gamma ray glows in being close enough, that is to say at high altitudes, like at Pic du Midi (France), or in Japan, where thunderstorms can occur at very low altitude. The probability to detect an event will be enhanced through increasing both the measurement time and the size of the detector. The entire high resolution data will be stored, allowing a post-processing analysis to detect even faint gamma ray glows.

3. Instrument Overview

The detection principle of XStorm (Figure 1) is based on scintillators associated with silicon photomultipliers (SiPMs). We use two types of scintillators: a Bismuth Germanium Oxide (BGO) crystal and a plastic scintillator of type EJ-276. BGO has been chosen given its characteristics adapted to the detection of high gamma ray fluxes in thunderstorms: fast (decay time of 300 ns), high density (7.13 g/cm³), and non hygroscopic. The plastic scintillator has been chosen considering its ability to perform gamma ray/neutron discrimination using a Pulse Shape Discrimination (PSD) method, that will be presented in the following. The weight being a strong constraint on balloon campaigns, we have chosen 1"-side cubic shape scintillators.

3.1. Design Philosophy and Overview

XStorm has been developed to obey specific constraints concerning balloon-borne instruments. It is contained in a steel and aluminum box with dimensions: 50 × 160 × 100 mm. It weighs less than 2 kg. Its power consumption is ~8 W. Its components are:

- one BGO scintillator: cubic shape with 1" side, packed in a light-tight box
- one plastic scintillator EJ-276 from Eljen Technology: cubic shape with 1" side, packed in a light-tight box
- two silicon photo-multipliers (SiPMs) C series, 30,035 from Onsemi. They are 3 mm × 3 mm and are composed of 4,774 microcells of 35 μm
- front-end electronics containing analog high-pass filters with a cutoff frequency of 27 kHz (that cancel out the continuous component of the signal), with one channel for each scintillator. Two different 12-bits ADCs are used, 40 MHz for the BGO channel and 200 MHz for the plastic channel that has a shorter decay time (tens of nanoseconds for the fast component). An FPGA (Xilinx ARTIX 7) and a Temperature Compensated X (Crystal) Oscillator (TCXO) are used respectively to analyze the signal and tag the arrival time of the particles in association with the pulse-per-second (PPS) signal fed by a GPS receiver
- a Raspberry Pi Zero used as a data-logger and a data analyzer

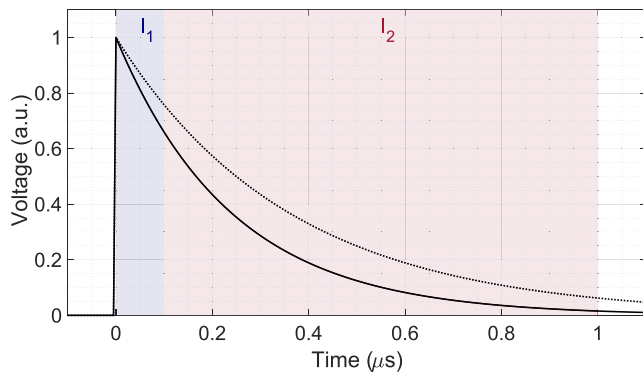


Figure 2. Integral calculations with the plastic channel. The first integral is calculated between 0 and 0.1 μs and the second one is calculated between 0.1 and 1 μs . This is part of the Pulse Shape Discrimination method.

- an Arduino board: a microcontroller board for the communication interface with the on-board computer (OBC) on Stratéole-2 balloons
- a power adaptation board on Stratéole-2 balloons

The light pulses produced by scintillators and SiPMs are filtered by the front-end electronics (high-pass filter) and then digitized by the ADCs. The FPGA analyzes this signal to detect pulses and calculate their integral. A threshold is chosen to detect pulses, and the integral is calculated in two parts over 1 μs for each pulse as shown in Figure 2. These two parts allow, on the plastic channel, to discriminate fast-neutrons from gamma-rays thanks to a PSD method, as explained in Section 3.3. The arrival time of the particle is measured within better than 1 μs precision (<600 ns from tests), relatively to the GPS signal used. For instance, the GPS receiver used for OREO is an Adafruit Ultimate GPS Breakout, and its precision is 10 ns (Adafruit, 2023). On the BGO channel, we use the two-part integral of the PSD method to reject spurious pulses possibly caused by highly energetic particles present at high-altitude. We refer to these events in Section 4.6.

In Table 1, one can find a summary of the performances of the spectrometer. The detector allows to discriminate gamma rays, neutrons, and electrons. The electron/gamma ray discrimination can be performed statistically by comparing the proportion of counts in each detector, knowing that electrons will be detected almost in the same proportion in both BGO and plastic scintillators, but gamma rays are detected more efficiently in the BGO. This means that for fluxes of both gamma rays and electrons, it will be difficult to determine the proportion of each type of particle, but the presence of electrons should however be identified.

3.2. Energy Range and Time Performance

The spectrometer is able to measure energies between ~ 400 keV and 20 MeV at 10°C , with a 20% resolution taken at FWHM at 511 keV. A background spectrum acquired over 4 hr on the ground at LPC2E, Orléans, France, has been plotted in Figure 3. Three lines from the background have been identified and used for the energy calibration: ^{40}K at 1.462 MeV, ^{214}Bi at 2.204 MeV, and ^{208}Tl at 2.615 MeV. To limit the effect of the temperature on the energy measured, namely the spectrum expansion when the temperature gets lower, a system of temperature compensation has been implemented to control linearly the SiPM voltages as a function of the temperature (see Section 4.3).

Data of every single particle detected is collected, that is to say that for every particle that goes through one of the scintillators and deposits energy above the threshold, both integral 1 and integral 2 described in Figure 2 and the arrival time within a 100 ns precision are saved. The quantity of data can therefore be sizable, according to the existing particle fluxes. Balloon campaigns with and without payload recovery are considered for XStorm. For balloon flights with payload recovery at the end, it is not a problem as SD cards with capacity of a few gigabytes are sufficient for several months of data. The analysis and event detection on the data can then be easily made after the campaign on the ground. But for flights with no possibility of recovery, data have to be transmitted through satellite communication that is limited. For this reason, we developed a special working mode, explained in Section 3.4, in which we collect low-resolution data in a survey, and collect the high-resolution data only

when an event has been detected by our event trigger system (here and in the following, we use the term “event” to refer to a TGF or a glow detected by the triggering algorithm).

The scintillation pulse integration window is fixed to 1 μs for both BGO and plastic channels. The spectrometer is a nonparalyzable detector, meaning that a particle arriving before the end of the integration window of the previous particle will not prolong the deadtime, it will just be ignored by the system. Count rates up to ~ 970 kHz can be recorded. Indeed, a deadtime of 1 μs due to the 1- μs integration window for each particle detection and an additional 30-ns deadtime, has been measured after the integration window for which the particles are not taken into account. Only very energetic particles detected

Table 1
Spectrometer Performances

Time accuracy	<600 ns UTC
Energy range	400 keV–20 MeV
Precision in energy	$\sim 20\%$ at 511 keV
Maximum count frequency	1 MHz
Particle discrimination	Photon/neutron (plastic) Photon/electron (statistically)

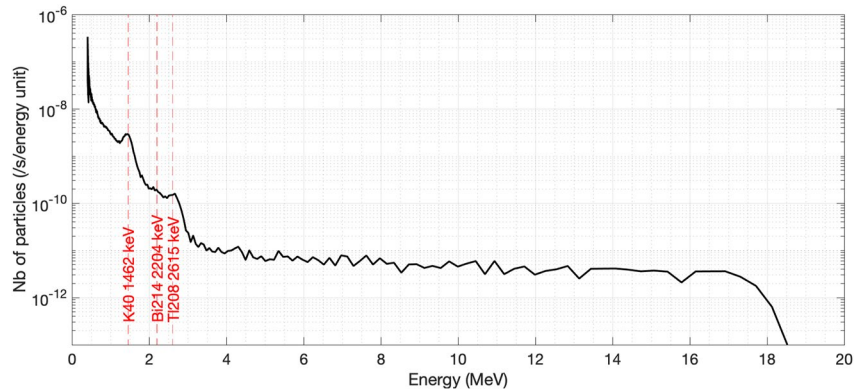


Figure 3. Background Bismuth Germanium Oxide spectrum acquired over 4 hr, on the ground at LPC2E, Orléans, France. Three lines from the background have been identified and used for the energy calibration: ^{40}K at 1.462 MeV, ^{214}Bi at 2.204 MeV, and ^{208}Tl at 2.615 MeV.

during test flights (probably protons) can blind the electronics for a few tens of microseconds. This phenomenon is also followed by other instrumental effects, discussed in Section 4.6. Pulse pile-up is possible for pulses separated by $<1 \mu\text{s}$. In this case, the number of counts detected and the energy of the pulse recorded will both be wrong. It is however possible to make an estimation of the presence of pile-up in analyzing the contribution of each part of the integral shown in Figure 2 (see Section 4.7).

3.3. Pulse Shape Discrimination (PSD) Method for Fast-Neutron Detection

Thermal neutrons usually require plastic scintillators loaded with elements having a high cross-section such as ^6Li , ^{10}B , or ^{113}Cd to be absorbed. This is not the case for the EJ-276, for which detected neutrons are fast neutrons, which interact efficiently with it. Different ionization mechanisms involve different decay time responses in EJ-276 plastic scintillator for gamma rays and neutrons (see Bertrand et al. (2015) for more details). In order to use this characteristic to discriminate neutrons from photons, without saving the whole signal, we use the PSD method that is based on the calculation of a ratio Q between the second part of the integral of a pulse and the total integral of the pulse:

$$Q = \frac{I_2}{I_1 + I_2} \quad (1)$$

where I_1 and I_2 are the partial integrals spanning over ranges illustrated respectively in blue and in red in Figure 2. Plotting Q as a function of the total integral of each pulse $I_1 + I_2$, involves a representation with two branches, one corresponding to photon pulses and the other to neutron pulses. This method has been used for instance in Cieřlak et al. (2019). The separation of the two branches is dependent on the choice of the limit between I_1 and I_2 . After measurement tests with a neutron source of Californium 252 (^{252}Cf), a separation at $0.1 \mu\text{s}$ appears to be the best choice for our detector. An example of a measurement with the neutron source is shown in Figure 4, where the two branches are identified. With this source and this technique, we measured 8% of neutrons, and 48% of gamma rays among the particles detected. 44% of the particles couldn't be identified as too low energy deposits may correspond to $Q = 0$. The discrimination can be performed for energy greater than 500 channels. According to Figure 11, it corresponds to $\sim 900 \text{ keV}$ for gamma rays. No energy calibration has been performed for neutrons yet.

Decay times assumed by the manufacturer (Eljen Technology) for EJ-276 scintillators are 13, 35, 270 ns for gamma rays and 13, 59, 460 ns for neutrons (Eljen Technology, 2023). The fact that there are three different decay times for one pulse is explained by the multiple processes producing the visible

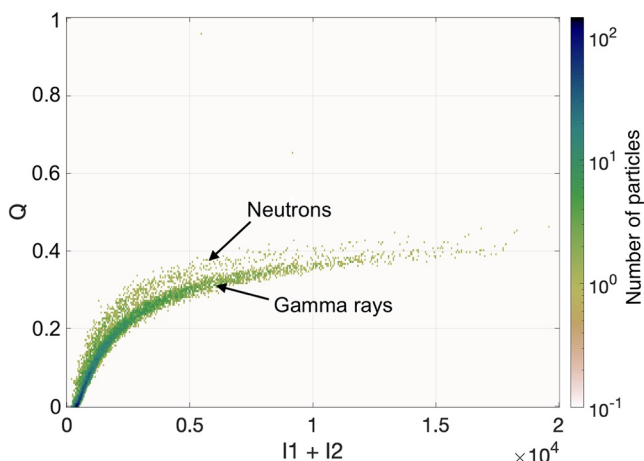


Figure 4. Pulse Shape Discrimination representation that allows to discriminate neutrons from gamma rays. Data have been measured with E-J276 XStorm exposed to a neutron source (^{252}Cf).

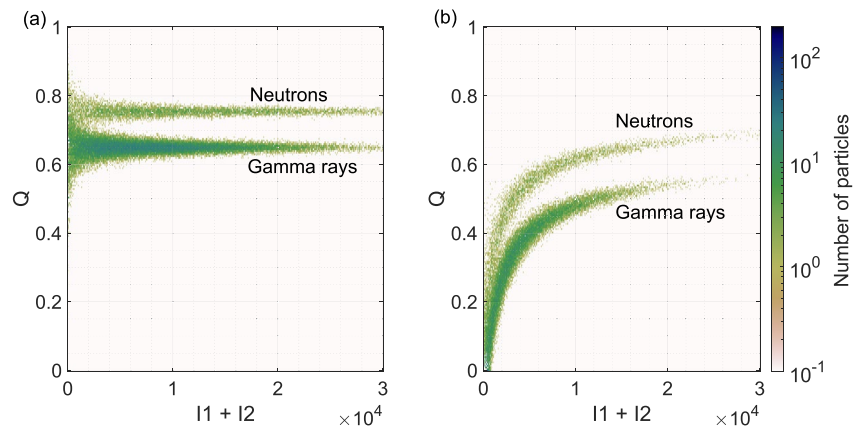


Figure 5. (a) Simulation of the Pulse Shape Discrimination (PSD) representation to discriminate neutrons from gamma rays. (b) Simulation of the PSD representation, with addition of a fixed level under which the pulse voltage is assumed to be zero (referred to as “fixed subtracted level” in the text).

photons (see Bertrand et al. (2015) for more details). However, SiPM filters extend the pulse duration and thus modify their characteristic decay time. Thus, to be closer to the electrical pulses measured by our scintillators and SiPMs, we acquired some pulses (~ 40) with XStorm plastic scintillator using an oscilloscope. They have been recorded during the experiment with the neutron source of Figure 4. Trying to fit them with a simple model $\propto \exp\left(-\frac{t}{\tau}\right)$ using only one decay time τ has given two type of pulses: the majority of them with a fitting decay time of ~ 240 ns, and 5 of them with a fitting decay time of ~ 360 ns. We developed a toy model to understand the influence of the different parameters of the detector on the PSD representation. For that we create pulses of different amplitudes with both decay times. We then add a Poisson noise on top of the exponential pulse. This means that the noisy pulse signal is chosen randomly, for each value, as drawn for the Poisson distribution of parameter lambda: $P(X = k) = \frac{\lambda^k}{k!} \exp(-\lambda)$ where $P(X = k)$ is the probability for X (the signal) to be equal to the value k , the initial signal being equal to λ . We plot the obtained theoretical PSD representation in Figure 5a. Two branches are clearly distinguishable. The upper one corresponds to the presumed neutrons. The proportion of neutrons and photons determined with Figure 4 is used for the simulation, namely among the identified ones there were 15% of neutrons and 85% of gamma rays.

Another example of neutron measurement is shown in Section 4.5, Figure 17, during a lightweight balloon flight. During the flight, neutrons represented about 1% of the particles detected on the plastic scintillator. Almost no cosmic neutrons are detected on the ground because of their expected rare presence at low altitude.

Both of these measured PSD representations show Q decreasing with the lower total energies, contrarily to the theoretical result shown in Figure 5a that shows Q almost constant (within the Poisson noise) as a function of the energy for a given particle type. This difference is due to the presence of a threshold and a fixed subtracted level implemented in the spectrometer front-end electronics. The threshold is the detection threshold mentioned before, which allows the particle detection only for pulses with a maximum greater than the detection threshold. The fixed subtracted level subtracts a constant value from the voltages that are lower than it. The pulses are then shifted to lower voltage values. Both values are illustrated in Figure 6. These characteristics have been implemented in the toy model in Figure 5b, and the decrease in the lower energies is clearly visible. The remaining differences between the theoretical and the measured figures come from differences in the decay times, the value of the threshold and of the fixed subtracted level, the spectra of the particles, and the photon/neutron proportion.

3.4. On-Board Software

In order to limit the quantity of data produced by the spectrometer, especially during balloon campaign with no payload recovery, a survey mode (“Survey Mode”) and an event detection system (“Trigger Mode”) have been developed. The Survey Mode allows to transmit to the ground low-resolution data when no “event” is triggered. The Trigger Mode allows to detect and send high-resolution data (arrival time and integrals of every particle) to the ground in case of the detection of an event (gamma ray glow or TGF). The Survey Mode is always

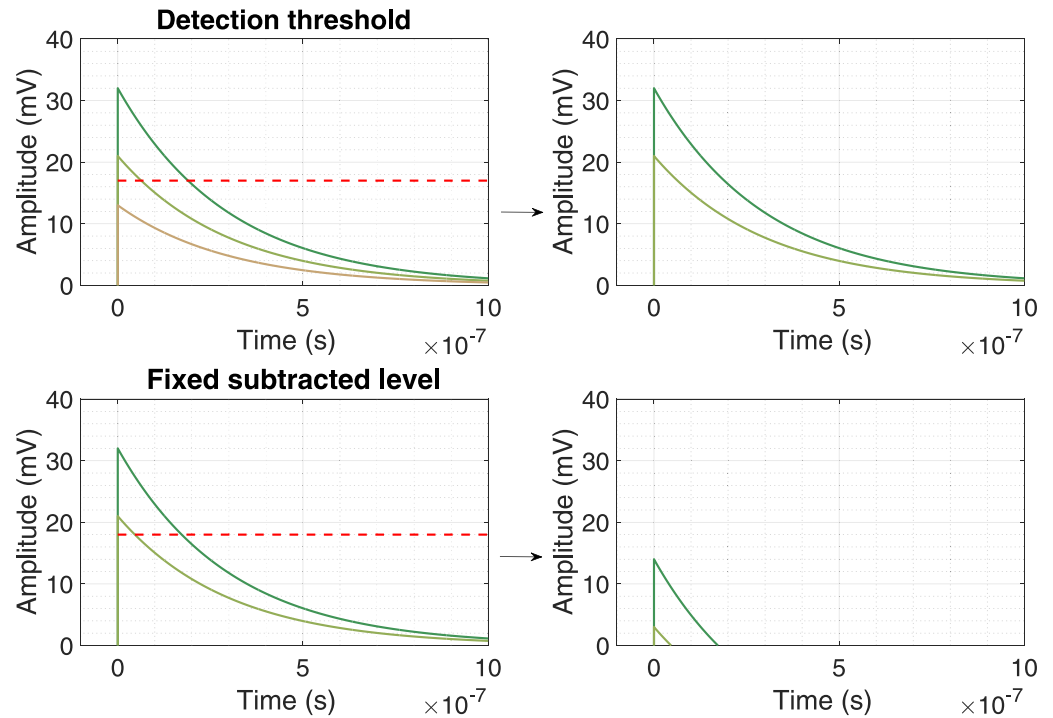


Figure 6. Illustration of the two variables implemented in the toy model to obtain Figure 5b. The detection threshold (17 mV here for instance, top panels) is used to detect pulses that exceed it. The yellow pulse is thus not detected, but the two green pulses are detected and not modified. The fixed subtracted level (18 mV here for instance, bottom panels) is a level that reduces the signal by 18 mV. The measured pulses are represented in the bottom-right panel.

running, and if an event is detected with the triggering system, the Trigger Mode is enabled and will provide high-resolution data for the duration of the event.

3.4.1. Survey Mode

The Survey Mode converts the high-resolution data containing each particle data (arrival time and two integrals) into more compact data. In this mode, only the following data are transferred to the ground: one low-resolution spectrum calculated every second with 10 energy bins, and one high-resolution spectrum calculated every hour with 1,000 energy bins. The Survey Mode can be used to verify the proper working of the instrument, for recalibration if needed, but also to identify events that would not necessarily be strong enough to meet the thresholds defining them as events (see next section) using on-ground data processing. For instance, see Section 5.3 for cases that would not be detected by XStorm triggering system using a 1-s detection bin, but could be detected through post-processing of the survey low-resolution data. The quantity of data purely acquired in the Survey Mode (i.e., with no triggered events) reduces from ~4 MB/hr to ~70 kB/hr. On Stratéole-2 campaign, the maximum down-link rate is 13 MB/day, to be shared by all the instruments of the gondola (usually 3 or 4 instruments on each gondola). Data are transmitted every hour during flights.

3.4.2. Trigger Mode

In the Trigger Mode, two different trigger thresholds have been developed to detect independently TGFs and gamma ray glows. Both triggers are based on a monitoring of the background radiation in real time. We assume that the number of particles detected in the scintillators over a given time bin follows a Poisson distribution law, even though the background is known to be not exactly Poissonian. In order to limit the number of false positives detected by the system, we use a criterion, which fixes the threshold for each type of event. Assuming a Poisson distribution of counts, the probability to have a number of counts k over a time bin of duration τ is:

$$P(X = k) = e^{-\lambda} \frac{\lambda^k}{k!} \quad (2)$$

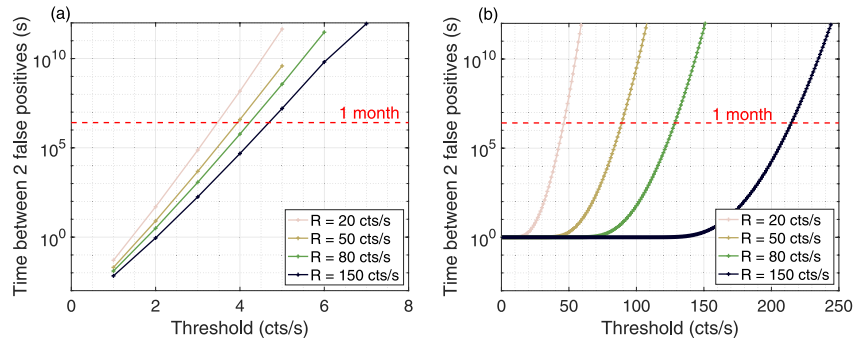


Figure 7. Time Δt between 2 false positives as a function of the threshold k and the radiation background R for (a) TGFs ($\tau = 100 \mu\text{s}$) and (b) gamma ray glows ($\tau = 1 \text{ s}$). The red dashed line corresponds to 1 month. The different count rates used come from a background radiation evaluation using the EXPACS model (Sato, 2015) and balloon measurements.

where $\lambda = R\tau$ is the mean number of particles detected over a duration τ and R is the mean number of particles detected per second. The probability to obtain more than k counts from the background over a time τ is then:

$$P(X \geq k) = \sum_{n \geq k} e^{-\lambda} \frac{\lambda^n}{n!} = 1 - \sum_{n < k} e^{-\lambda} \frac{\lambda^n}{n!} \quad (3)$$

The high-energy background can cause any numbers of counts over a given duration Δt with a likelihood quantified as above. These background-associated events ($X \geq k$) are referred to as false positive events. The duration between two false positives is then:

$$\Delta t = \frac{\tau}{P} \quad (4)$$

Given the duration on Strateole-2 flights (a few months), we typically fix that it is acceptable to have one false positive per month, therefore we choose $\Delta t = 1$ month. The thresholds are then depending on the number of counts from the background radiation R . According to balloon measurements presented later in Section 4, the typical background count rates range between ~ 20 and ~ 150 cts/s.

Concerning TGFs, the typical time duration is $\sim 100 \mu\text{s}$ (e.g., Fishman et al., 2011), therefore we use $\tau = 100 \mu\text{s}$. Figure 7a shows Δt as a function of the threshold k and the background radiation R with $\tau = 100 \mu\text{s}$. One can see that Δt does not vary significantly as a function of the background radiation, and therefore, given the observed background in the lower stratosphere (see Figure 17) we fixed the threshold constant at 5 counts/100 μs . One can note that changing the TGF threshold of 1 count would lead to a Δt change of 2–3 orders of magnitude.

Concerning gamma ray glows, the time duration can presumably vary from seconds to tens of minutes. Thus, to be able to detect even the shortest glows we typically use $\tau = 1 \text{ s}$. Figure 7b shows Δt as a function of the threshold k and the background radiation R for $\tau = 1 \text{ s}$. Δt varies significantly as a function of the background radiation level, and therefore we developed a system to monitor the background radiation and dynamically fix the threshold based on it, in real time, so as to always keep $\Delta t = 1$ month. For instance, if the background radiation level measured is 80 cts/s, the gamma ray glow threshold will be fixed to 128 cts/s.

When one or the other of the thresholds has been overtaken, the on-board software (Trigger Mode) will record and send the high-resolution data to the ground through satellite link, until the end of the event. For gamma ray glows, the event is not closed until the count rate does not come back under the gamma ray glow triggering threshold. It is worth mentioning that the value of τ and the number of counts for the TGF threshold can be changed during flight using a telecommand (through the balloon satellite link), and can thus be adapted after getting the first data in flight.

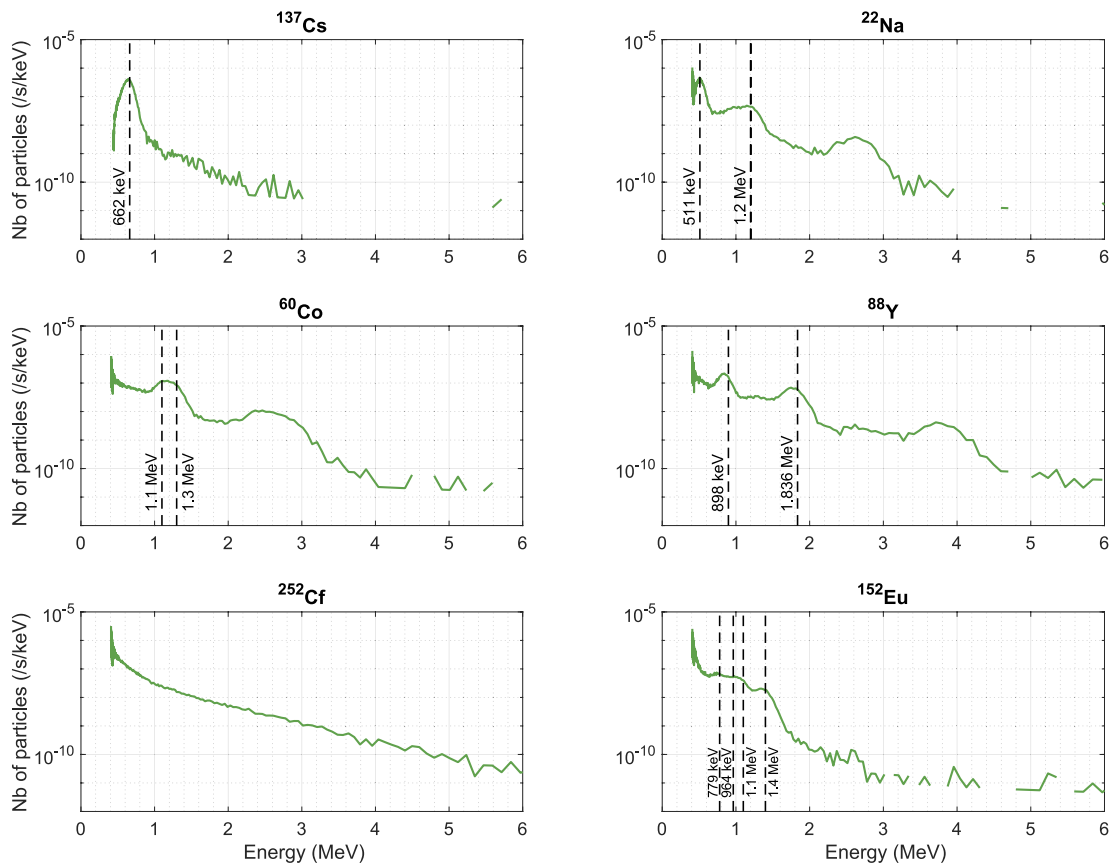


Figure 8. Energy spectra acquired with different radioactive sources. The expected gamma ray lines are shown by black dashed lines. Spectra have been acquired for duration between 1 min (for sources close to the detector) to 15 min (for ^{152}Eu).

4. First Measurements

4.1. Measurements of Radioactive Sources

XStorm's BGO has been calibrated using several radioactive sources: ^{137}Cs , ^{22}Na , ^{60}Co , ^{88}Y , ^{252}Cf , and ^{152}Eu . The calibrated spectra acquired with these sources are shown in Figure 8. The expected gamma ray lines from these sources are shown as black dashed lines. Measurements of ^{22}Na , ^{60}Co , and ^{88}Y have been made very close to the source (<1 cm). This particular configuration explains the “additional” lines observed in these spectra for higher energies. When the source is close to the detector, it increases the probability to detect two gamma photons in the same time range (here 1 μs). In this case, the energy measured will correspond to the sum of the energy of both particles. This phenomena is called *coincidence summing*, creating *sum peaks*, and is also referred to as *pile-up* in a more general context. The resolution of the spectrometer being only $\sim 20\%$, it is not possible to distinguish two close lines, for instance the two lines of ^{60}Co at 1.1 and 1.3 MeV. ^{22}Na , with the line generated at 511 keV, confirmed that we would be able to detect this energy in case of the measurement of a TGF afterglow for instance, as reported by Enoto et al. (2017). The ^{252}Cf source is a neutron source, used in particular to test and calibrate the PSD method, and does not show any gamma ray lines (^{252}Cf is known to emit gamma rays following a continuous energy spectrum). The corresponding calibration is shown in Figure 9.

The calibration process of XStorm's EJ-276 is different from XStorm's BGO. Indeed, due to the low atomic number and density, the main dominant photon interaction is Compton effect. Therefore, instead of using the photoelectric peak, the Compton edge is used as a calibration reference. In order to improve the determination of the Compton edge channel, we modify the original spectrum (background + source) in order to get only a relative spectrum (shown in Figure 10, for ^{22}Na , ^{60}Co , and ^{88}Y spectra) with:

$$\text{Relative spectrum} = \frac{\text{Original spectrum} - \text{Background spectrum}}{\text{Original spectrum}} \quad (5)$$

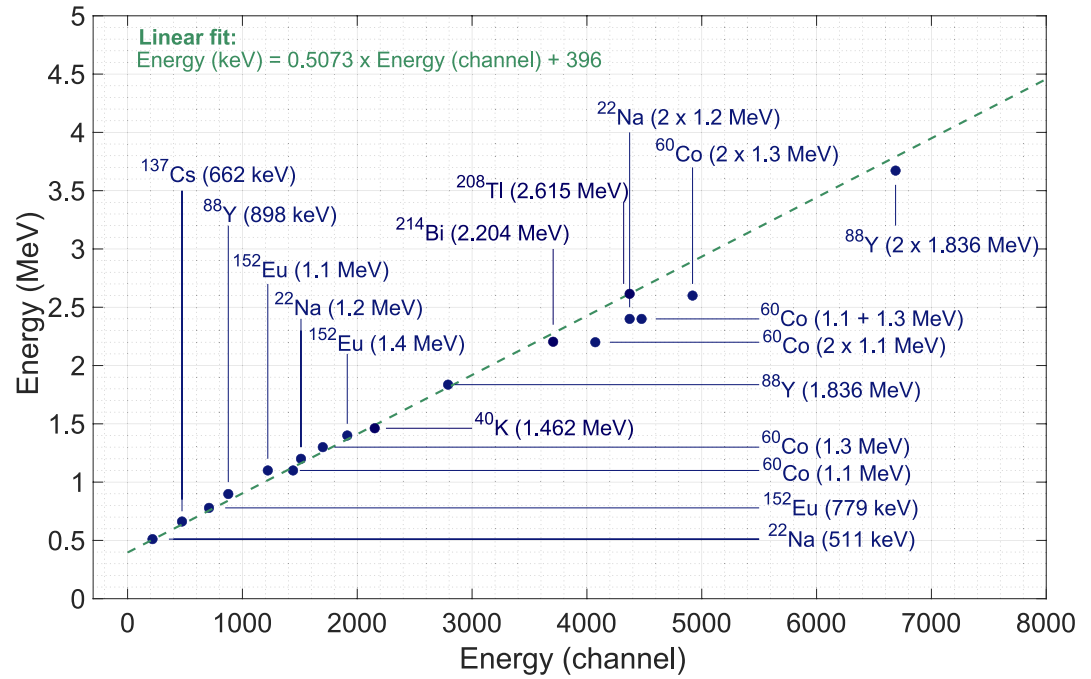


Figure 9. Spectrometer calibration for the Bismuth Germanium Oxide channel based on various radioactive source lines below channel 3000. Above channel 3000, the spectral structures identified correspond to sum peaks and are not as resolved as standard lines. They are indicated here to demonstrate the validity of the calibration up to 4 MeV. At higher energies, the linearity of the detector is verified through the detection of muons (Section 4.2).

There should be no photo-contribution beyond the Compton edge. Therefore, the channels corresponding to the beginning of the drop in the relative spectra corresponds to the Compton edge, as represented by the vertical lines in Figure 10. With this approach, we were able to determine the Compton edges of several sources, shown in Figure 11. The piled-up Compton edge of the ¹⁵²Eu line at 2 x 1,192 keV has also been detected. The coincidence summing is indeed not exclusive to photoelectric effect.

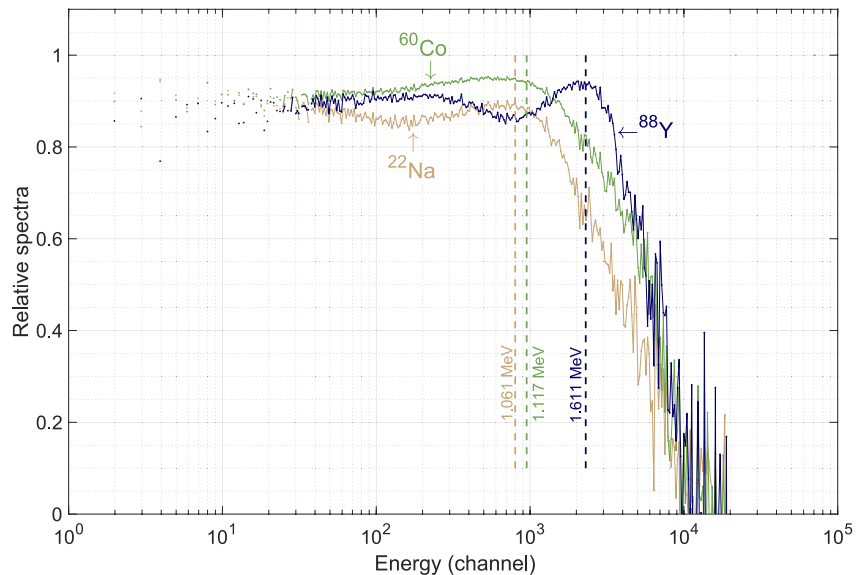


Figure 10. Spectrometer calibration for the EJ-276 channel using ²²Na, ⁶⁰Co, and ⁸⁸Y spectrum. The dashed lines correspond to the Compton edge positions, with the corresponding energy.

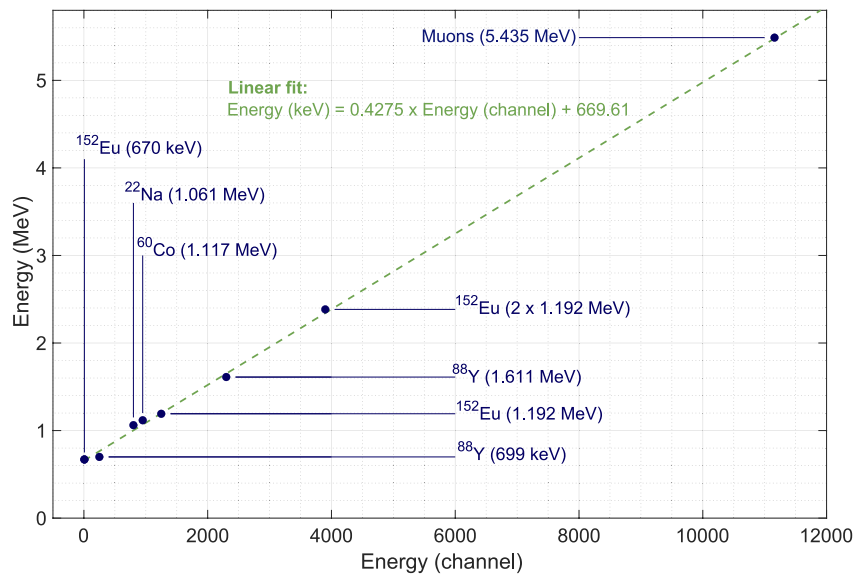


Figure 11. Spectrometer calibration for the EJ-276 channel using Compton edge channels, since photoelectric peaks cannot be identified. At higher energies, the linearity of the detector is verified through the detection of muons (Section 4.2).

4.2. Linearity of the Detector at Higher Energy: Muon Peak

Cosmic rays produce muons that can be detected by scintillators on the ground, and allow the energy calibration for higher energies than usual gamma ray sources. Muons detected on the ground are considered as minimum ionizing particle because of their mean energy of 4 GeV (Workman, 2022). XStorm BGO is a 2.53 cm-large crystal, in which muons deposit 1.26 MeV cm²/g (Groom et al., 2001). The BGO density is 7.13 g/cm³. Then, one finds that the muons should deposit about 22.7 MeV in XStorm's BGO scintillator.

The measurement of the muon peak is shown in Figure 12, as expected around 23 MeV, with a resolution at FWHM of 46%. This spectrum has been acquired over 36.5 hr, with a smaller gain than usually used for XStorm BGO. Using both BGO and plastic scintillators that are stacked one over the other, one can determine *coincidence*

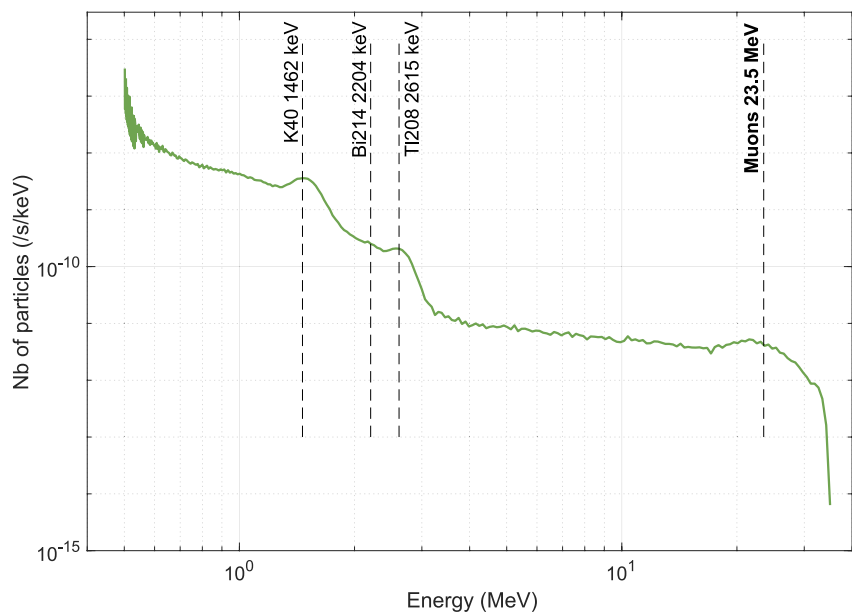


Figure 12. XStorm Bismuth Germanium Oxide (BGO) spectrum acquired using low gain. The black lines correspond to the expected deposited energies by natural radioactivity and muons in the BGO scintillator at ground level.

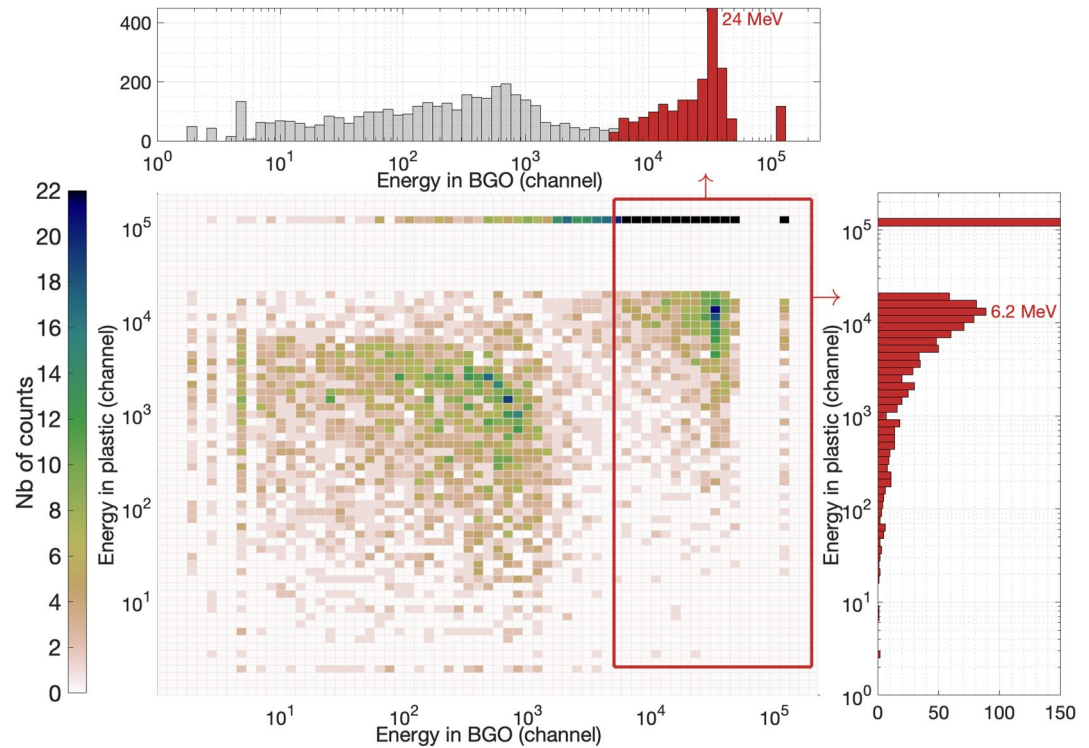


Figure 13. Energy spectrum of coincident counts in Bismuth Germanium Oxide (BGO) and plastic scintillators. Using BGO calibration, the peak of the deposited energy by muons in the BGO is found to be 24 MeV. Using plastic calibration, the peak of the deposited energy by muons in the plastic is found to be 6.2 MeV, in good agreement with what expected from theoretical prediction of 5.4 MeV.

counts, that correspond to counts detected in both BGO and plastic scintillator within $<1 \mu\text{s}$, and that could be the same particle detected in both scintillators (mostly muons at ground level). One found out that coincidences represent $\sim 45\%$ of BGO counts around 23 MeV, whereas it represents only $<20\%$ of them for energies below 20 MeV.

Through the coincidence counts, we use muon counts in the BGO channel to identify the energy of muons on the plastic channel (see Figure 13). Using the calibration (Figure 11), we determine a mean energy of muons of 6.2 MeV in the plastic scintillator. Since we do not know the exact chemical composition of the plastic, we chose from Groom et al. (2001) a plastic with nearly the same density and same proportion of C and H. This plastic is the polyvinyltoluene where muons loose $1.956 \text{ MeV cm}^2/\text{g}$, and EJ-276 density is 1.096 g/cm^3 . EJ-276 is 2.53 cm-large, then we find that muons should deposit about 5.4 MeV, which is close to the value determined with the calibration. This value is in very good agreement with the calibration shown in Figure 11. The discrepancy with the value found experimentally using the above method is believed to be caused by the rather low resolution of the coincidence peak found in the plastic scintillator. The angular distribution of muons in $\cos(\theta)$ also adds to the discrepancy.

4.3. Temperature Dependency

The spectrometer behavior is dependent on the temperature. Three factors are playing a role: the BGO/SiPM coupling, the SiPM gain, and BGO light yield. On XStorm BGO, the temperature-dependency of the spectrometer gain implies an expansion of the spectrum to high energies at low temperature. This is due first to the better efficiency of the scintillator/SiPM coupling under low temperatures and second to the breakdown voltage of the SiPM that is lower at low temperatures. In fact, when the SiPM voltage is kept constant, the overvoltage (voltage difference between the *breakdown voltage* and the voltage applied) is greater, and the SiPM gain is also greater.

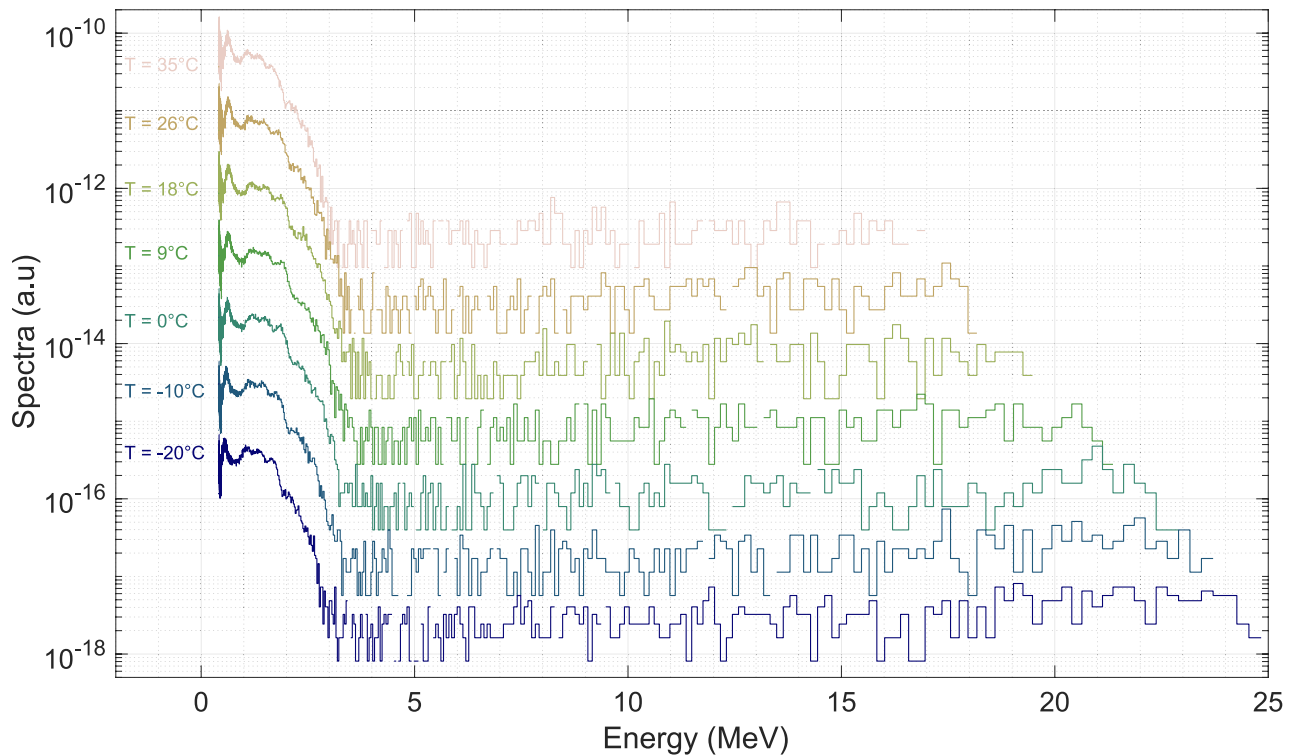


Figure 14. Spectrum stability at various temperatures owing to the SiPM gain linear adjustment. A unique energy calibration is used for all the spectra. The high-energy cut-off in the spectrum is also evident. At low temperatures, higher energies are detected without saturation (see text).

During preliminary tests, this spectrum expansion was so intense that some pulses saturated, thus populating and polluting lowest energy bins. The integral of a saturated pulse, that is to say whose top has been cut out, is equal to the integral of non saturated pulses of a lower energy, which involves a folding of the spectrum at high-energy. We have thus implemented a saturation bin, which contains the number of saturated pulses to prevent spectrum folding.

We also implemented a linear dependence of the SiPM supply voltage on the temperature to stabilize the gain. This linear function is sufficient to limit the drift of the spectrum for temperatures between -20°C and $+40^{\circ}\text{C}$, corresponding to temperatures that could be reached during balloon flights. This correction is effective and can be seen in Figure 14, where a unique energy calibration is used to represent all the spectra. Lines for energies <2 MeV are at the same position for temperature between -19°C and 35°C .

In Figure 14, one can also see that the BGO spectrum high-energy cut-off depends on the temperature, even after implementation of the temperature correction. This is not the effect we referred to in the beginning of this section. The energy spectra have been acquired in the laboratory, using the same temperature chamber. At low temperature, using the same energy calibration, the spectra are going higher in energy, meaning that higher energies are detected. This can be explained by the fact that at low temperatures the decay time is extended in crystals such as BGO (Gironnet et al., 2008; Zucchiatti et al., 1989). We have confirmed this effect by measurements of the decay time at different temperatures using pulses seen with an oscilloscope after the couple scintillator/SiPM. We measured a decay time of ~ 0.77 μs at 5°C and a decay time of ~ 1.46 μs at -30°C . With a longer decay time, higher energies can be deposited in the BGO without saturating the signal. This is totally due to the fact that we measure the integral of the pulse to estimate the energy. Pulses are scaled linearly using their integrals as references, and thus, for the same voltage saturation threshold, a longer decay time at lower temperature will allow the detection of higher pulses in amplitude, thus in energy. This effect is illustrated in Figure 15, which shows that the detection range is extended to higher energies for a lower temperature.

For the plastic scintillator, we have verified that the decay time does not depend on temperature. The gain is kept constant for the plastic channel.

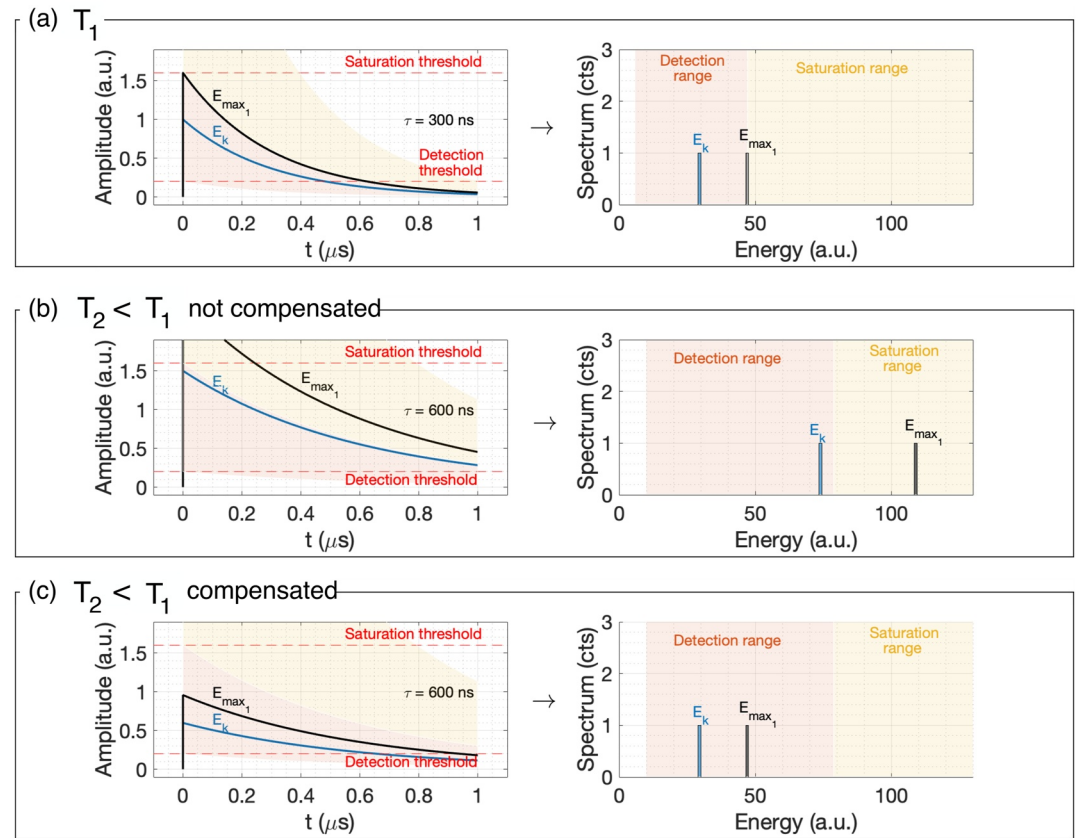


Figure 15. Detection ranges (shaded red) and saturation ranges (shaded yellow) as a function of the temperature. Panels (a) represent two pulses (blue and black lines) going out of the scintillator/SiPM couple. They have integrals (energies) equal to E_k and E_{\max} at a temperature T_1 . Panels (b) represent the same energy pulses at a temperature $T_2 < T_1$, without applying the temperature correction on the SiPM supply voltage explained in Section 4.3. One can see that the lower temperature implies a greater amplitude and a longer decay time. Panels (c) represent the same energy pulses at the temperature T_2 , but with the temperature correction applied, to keep the spectrum constant as a function of the temperature. The amplitude is then lower compared to pulse amplitude at T_1 as the integral is the same but the decay time is longer. The detection range corresponds to the pulses with amplitudes up to the saturation threshold (red shaded region in each panel). The position in the energy spectrum of each pulse for each situation is represented in the right panels, using the same colors. Whereas the black pulse in panel (a) was the maximum of the detection range (~ 50 a.u.), in panel (c) it is not anymore because of the longer decay time. The detection range is extended to higher energies for $T_2 < T_1$, the maximum energy of the detection range is then ~ 80 a.u.

4.4. Underestimation of the Energy for High Count Rates

Using a pulse generator, by-passing the couple scintillator/SiPM, we sent one artificial pulse with different count rates to compare the evaluation of the energy by the electronics. For count rates greater than ~ 100 kHz, the energy is increasingly underestimated with the increase of the count rate, as shown in Figure 16. For instance, at 500 kHz, the energy measured corresponds to $\sim 70\%$ of the real energy. At 1 MHz, the energy measured corresponds to 50% of the real energy. This phenomenon is produced by the front-end electronics, composed of analog high-pass filters that cancel out the continuous component of the signal. At high-frequency rates, this continuous component is not efficiently filtered, and a bias is introduced in the energy calculation. Knowing the filter response, it is in principle possible to estimate the impact of this effect for measurements with count rates greater than 100 kHz.

4.5. Lightweight Balloon Measurements in Fair Weather

Several radiosonde-type balloon flights have been made in fair weather conditions to validate the spectrometer's behavior. This balloon type can carry up to ~ 3 kg of scientific payload (depending on the exact flight chain configuration and the civil aviation authority) for a flight that lasts about 2–3 hr. The balloon goes up to

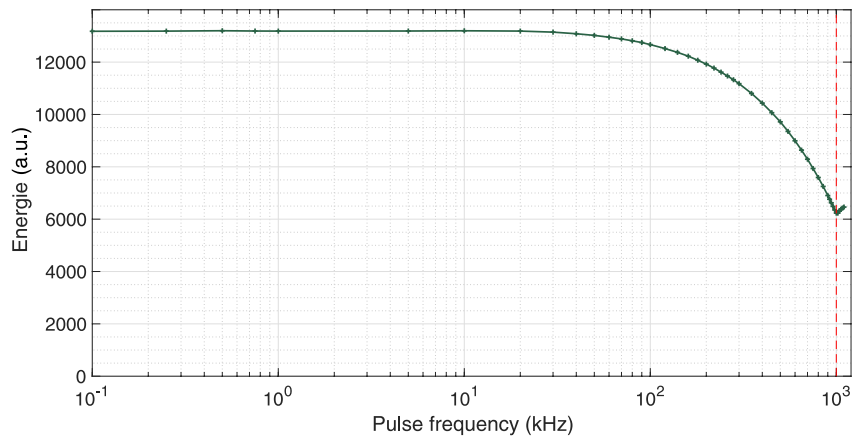


Figure 16. Measured energy of a pulse as a function of the count frequency. Pulses used are identical and generated by a pulse generator. The energy is attenuated from count frequency of ~ 100 kHz.

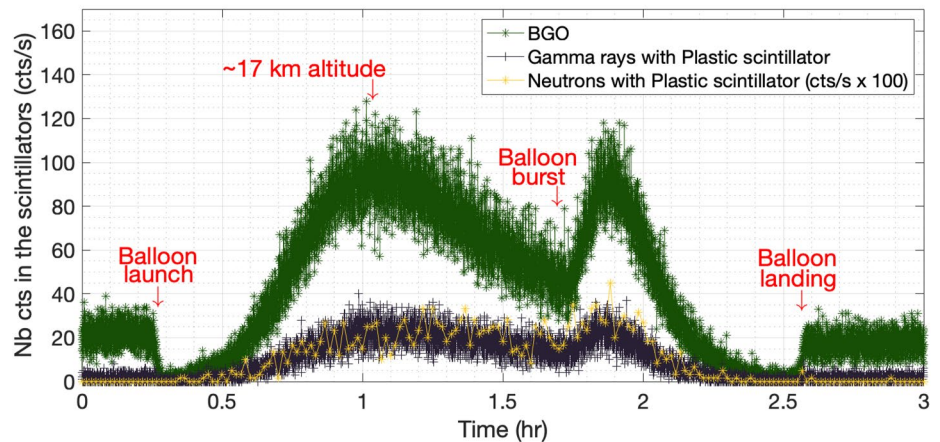
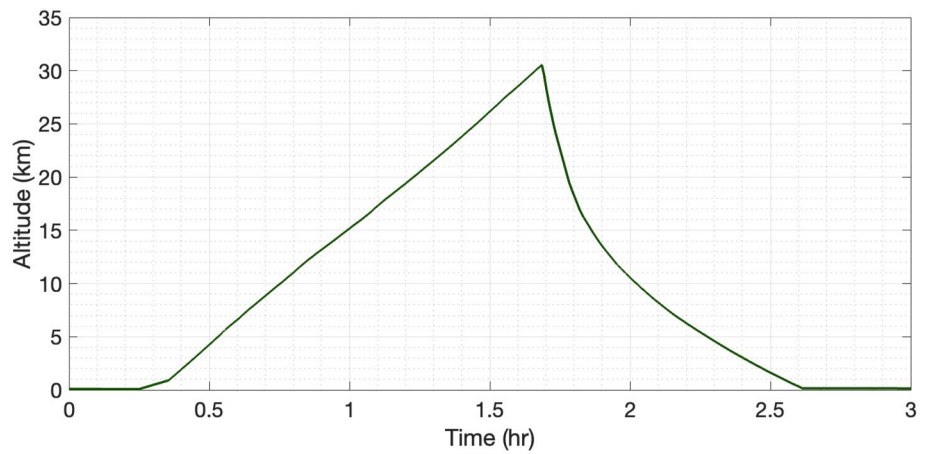


Figure 17. Data from a lightweight balloon flight in fair weather, launched on the 7 October 2021 at Aire-sur-l'Adour/France. (top) Altitude of the lightweight balloon as a function of time. (bottom) Number of particles detected by XStorm as a function of time.

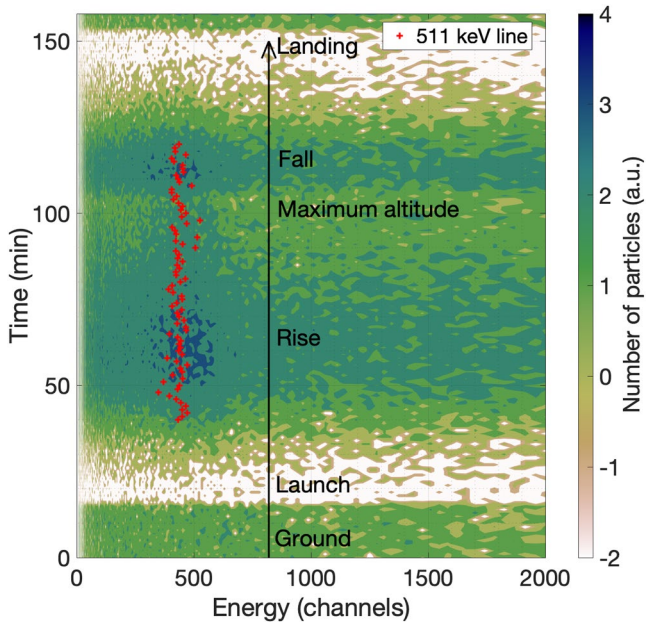


Figure 18. Energy spectrum (low-energy part) as a function of time during the same balloon test flight as in Figure 17. The 511 keV-line is emphasized in red along the duration balloon flight. The gain is well-stabilized along the rise and the fall of the balloon, despite the temperature variation between 15 and -5°C at the maximum altitude.

~ 30 km altitude, bursts, and goes down below a parachute (Figure 17, top). The payload is recovered at the end of the flight.

We present the number of particles detected by XStorm as a function of time with the corresponding altitude in Figure 17. Both BGO and plastic channels are represented, with a discrimination between gamma rays and neutrons made using the PSD method on the plastic channel (see Section 3.3). The background radiation level on the ground before launch and after landing is due to natural radioactivity from the soil. Then, the rate of detected particles is dependent on the altitude, with a maximum rate around 17 km, which is called Regener-Pfotzer maximum (Regener & Pfotzer, 1934). This maximum depends on the latitude and is lower at lowest latitudes. The balloon bursted at 33 km. The number of neutrons in Figure 17 is multiplied by one hundred to make the interpretation of the figure easier. Almost no neutrons have been detected on the ground, that is consistent with the proportion of neutrons (>1 MeV) at ground level estimated by EXPACS (Sato, 2015) to be lower than 10^{-2} neutrons/s/cm² (in Toulouse, France, at <300 m of altitude), and the fact that natural radioactivity is not expected to produce significant neutron count rate. Neutrons (>1 MeV) are estimated by EXPACS to represent $\sim 20\%$ of the particles detected at 17 km of altitude, with ~ 2 neutrons/s/cm².

This flight also validated the gain stabilization method. At high altitudes, 511-keV photons produced from the annihilation of secondary cosmic positron can be seen. Figure 18 shows the low energy part (<1 MeV) of the energy spectrum as a function of time during the flight. Using a Gaussian fit over one energy spectrum per minute, we plotted in red the energy channel corresponding to the center of the 511-keV line. It shows that XStorm gain is well stabilized by the method explained in Section 4.3, despite the temperature variation, going from 15°C on the ground and reaching -5°C at 30 km.

4.6. Instrumental Effect Caused by Very Energetic Particles

During balloon flight tests in fair weather conditions, numerous events (~ 500 per flight) with hundreds of counts occurring within hundreds of microseconds have been recorded at high-altitude. One of these events is shown in Figure 19. The typical count sequence is always the same, one saturated count followed by 50–70 μs without signal during which the detector is blind, and afterward approximately one hundred counts within 30–50 μs . The shape followed by count energies illustrated in Figure 19 is indicative of a strong instrumental effect that does not seem physical. These events have been recorded mostly at high-altitude, only few have been recorded on the ground, less than 5 over several weeks of measurements. On the other hand, the number of these events detected during a balloon flight is very high, 474 events over a 2.5 hour flight, that corresponds to 1 every ~ 20 s.

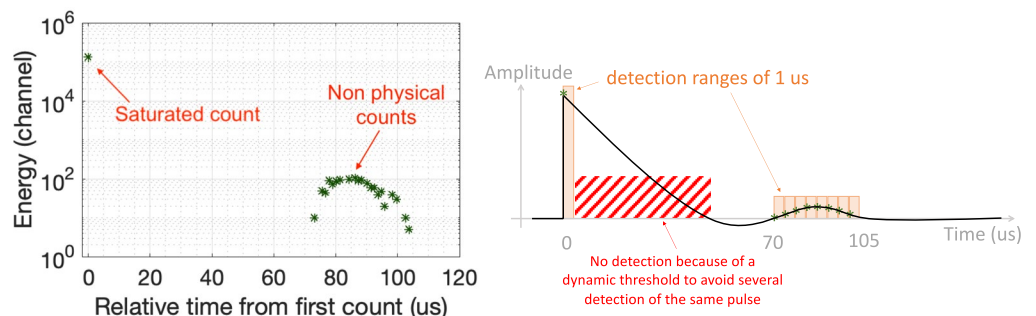


Figure 19. (left) Instrumental effect detected during a balloon flight with XStorm. (right) Schematic representation of the waveform that could have produced the instrumental effect. The spurious counts could be produced by the signal bounce.

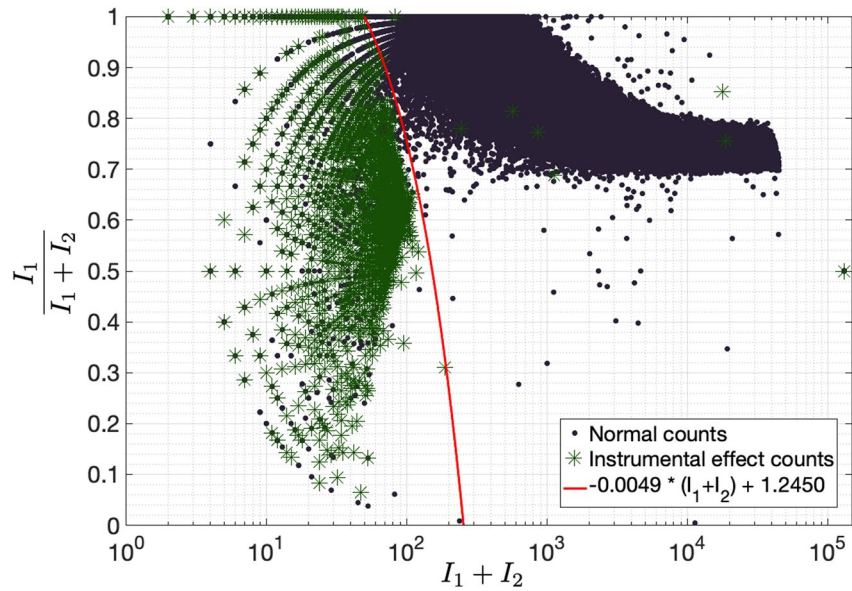


Figure 20. Representation of the Pulse Shape Discrimination on the Bismuth Germanium Oxide scintillator channel during a balloon flight. Black points represent “normal” counts. Green stars represent the counts generated by instrumental effects. The red line is the separation between the two regions (“normal counts” and “instrumental effect counts”) given by the inequation (6). See Section 3.3 for a definition of the axes' labels.

Investigating how these events can be produced in the spectrometer, we found that we could reproduce similar effects using electric pulses with a very high amplitude and duration as an input signal, that is, instead of the SiPM output signal. We realized that the electric potential before the ADC was going negative, and coming back as a bounce to a positive signal. The signal waveform is illustrated in Figure 19 (right). This last positive part corresponds to the counts detected around 90 μ s (about one per microsecond i.e., one in each detection time-window). According to Geant4 simulations for protons at 30 km of altitude (Sato, 2015), in a 2.53 cm-side BGO, we estimate that a proton can deposit up to \sim 100–200 MeV in the BGO, sufficient to produce a very high amplitude pulse. We propose to estimate the minimum deposited energy needed to match the rate of 1 event per 20 s, measured with XStorm BGO. Using the proton spectrum given by EXPACS (Sato, 2015) at 30 km as an input flux in the BGO, and keeping track of the energy deposited using Geant4, we estimate that this minimum deposited energy producing those instrumental effects at the same rate is \sim 110 MeV.

This instrumental effect has the particularity to validate the criterion chosen to detect TGFs (Section 3.4.2). Therefore, our event triggering protocol leads these instrumental effects to be detected as TGFs every \sim 20 s, potentially associated with a large amount of data saved and an overuse of the satellite communication link during a balloon flight. For this reason, we had to find a way to discriminate TGFs from these instrumental effects. Despite the fact that it seems visually easy to do this discrimination, the diversity of the parameters such as the time between the saturated count and the following counts group, the number of counts in the following count group, the energies of the counts, etc., leads to the difficulty to find specific criteria to uniquely identify them. The PSD method was not used on the BGO channel. Using an adapted separation ratio between the two calculated integrals (illustrated in Figure 2), we can use a method of PSD on the BGO scintillator channel to identify spurious events. After tests using different ratio between 10% and 90%, we found out that the method was more efficient to discriminate particles and instrumental pulses using a ratio of 60% for I_1 .

Figure 20 shows a representation of the PSD on the BGO scintillator channel during a balloon flight. We can clearly identify two groups of counts, according to their type. Instrumental effect counts are identified through the TGF events triggering protocol, since no TGF is expected to occur in fair weather conditions. We thus assume that spurious counts satisfy the following inequality:

$$\frac{I_1}{I_1 + I_2} < -0.0049 \times (I_1 + I_2) + 1.2450 \quad (6)$$

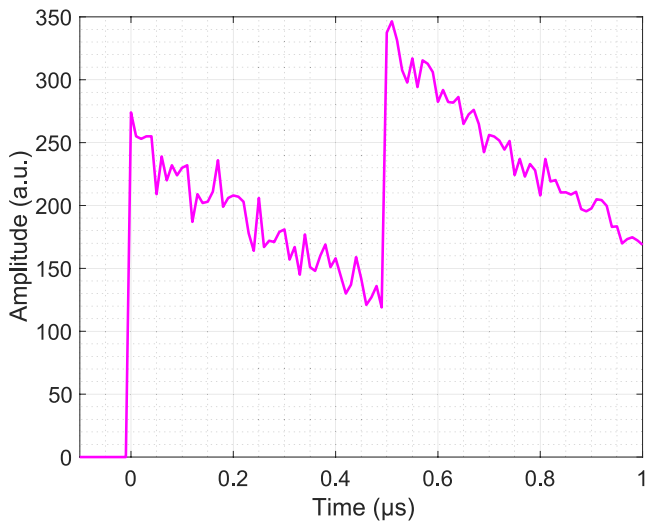


Figure 21. Example of piled-up pulses simulated with our toy model. The second pulse is observed before the end of the integration window of the first pulse.

where I_1 and I_2 are the two integrals defined in Figure 2 but with a separation at $0.6 \mu\text{s}$.

This criterion is used as follows. The event triggering protocol selects all counts that satisfy “more than 5 counts in $100 \mu\text{s}$ ” (see Section 3.4.2). Every count belonging to this group is classified as “normal” or “instrumental” count with the inequation (6). If more than 90% of the counts within one event are estimated to be instrumental effect counts, we consider that the counts do not come from a TGF detection. This method has been tested in flight, and has shown a 100% rejection rate of the spurious instrumental effects.

4.7. Pulse Pile-Up

The detection of TGFs in close proximity is likely to produce a significant amount of pile-up, and therefore such “true” events are at risk of being rejected as well. In order to improve the method presented in the previous section, and to find a method to detect the presence of pulse pile-up, we used the same toy model presented in Section 3.3. On this channel, the separation ratio is fixed to $0.6 \mu\text{s}$. Real pulses are modeled by exponential pulses and Poisson noise, in black in Figure 22. We model the spurious pulses using square pulses of low amplitude and Poisson noise, visible in green in

Figure 22. We model piled-up pulses in magenta in Figure 22. For the latter, we model two exponential pulses in less than 1 microsecond, with different amplitudes and Poisson noise, using different delay between the two pulses. An example of piled-up pulses is shown in Figure 21.

One can see that the results of the toy model are similar to the measurement presented in Section 4.6 for real and instrumental counts. Moreover, we found out that the PSD representation on the BGO channel can be used to test the presence of pile-up in the data, owing to the different ranges covered by piled-up and single pulses in Figure 22, despite the fact that the magenta and black regions are overlapping and could imply difficulties to distinguish piled-up pulses from single pulses.

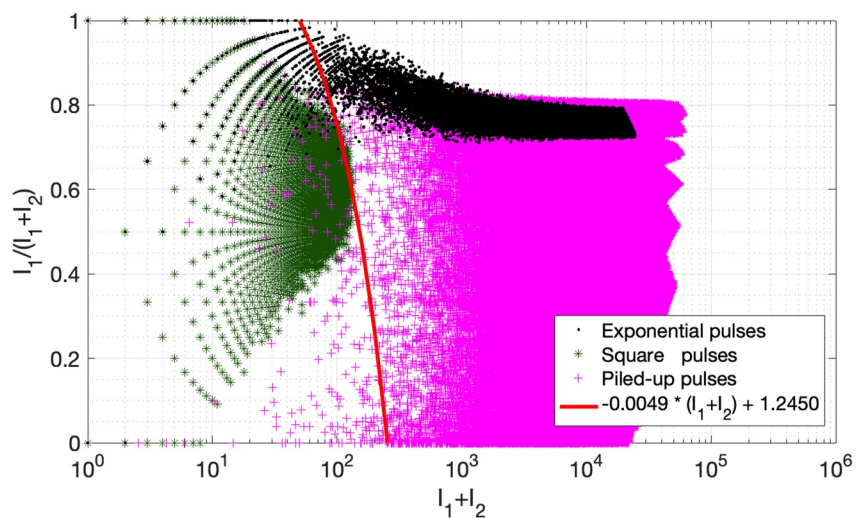


Figure 22. Representation of the Pulse Shape Discrimination with simulated pulses. Black dots correspond to exponential pulses, namely “real pulses.” Green stars correspond to square pulses, representing pulses from instrumental effects (see Section 4.6). Magenta crosses correspond to several exponential pulses in less than $1 \mu\text{s}$, namely piled-up pulses, for different configuration. See Section 3.3 for a definition of the axes’ labels.

5. Detectability of Gamma Ray Glows and TGFs

In this section, we present calculations and simulations to determine how and where a gamma ray glow can be detected using XStorm on balloon campaigns such as Stratéole-2 and OREO. We also present calculations on the probability to detect a TGF during a Stratéole-2 balloon flight. In this section, we assume a stable gamma ray glow, in order to evaluate only the detectability without taking into account the occurrence probability. By stable we mean that the gamma ray glow last longer than the size of the detection bin. The main calculations concerning gamma ray glows in this section are based on the gamma ray glow detected by Kelley et al. (2015). This detection has been chosen because it represent a high-altitude in situ measurement, supplying the electron flux at the source, easily transferable to different configurations. As it can be considered as bright, we can consider that it is a case setting a limit on the detector sensitivity.

5.1. Simulation of Photon Propagation for Gamma Ray Glows

We simulate the propagation of photons in the Earth atmosphere, from source altitudes between 1 and 20 km. The photon propagation is simulated using a Monte Carlo transport code, based on Østgaard et al. (2008) (for further explanations, see Pallu et al., 2021). A standard scale height of 8.2 km is used for the density profile of the atmosphere. Only the propagation of photons is simulated in this work (no Monte Carlo simulation of electrons and no electric field is used), and we assume an initial gamma ray spectrum corresponding to a standard RREA spectrum with a 7.3-MeV cut-off (e.g., Dwyer et al., 2012). The MOS mechanism is not addressed in the present work.

To evaluate the flux attenuation as a function of altitude, we simulate point sources, with all velocities aligned either upward or downward (emission angle set to zero). Gamma ray glows are expanded sources and are therefore evaluated using the ratio of the final to the initial photon fluxes, corresponding to the ratio of the number of photons received at a given altitude to the initial number of photons. Two different configurations will be used, one with initial photon velocities directed upward, and the other one with initial photon velocities directed downward, to model different charge structure cases in thunderstorms. The gamma ray flux estimated with Kelley et al. (2015)'s is for photons >1 MeV. XStorm detects gamma rays >400 keV. The proportion of photons transmitted at altitude h , called P_h , presented in this work is then calculated as:

$$P_h = \frac{N_{\text{ph}}(E > 400 \text{ keV}, z = h)}{N_{\text{ph,init}}(E > 1 \text{ MeV})} \quad (7)$$

where $N_{\text{ph}}(E > 400 \text{ keV}, z = h)$ is the number of photons that reach the observation altitude h with energies >400 keV, and $N_{\text{ph,init}}(E > 1 \text{ MeV})$ is the number of photons with energies >1 MeV that were produced at the source altitude. For information, in the Monte Carlo simulation, photons are simulated from $E > 10 \text{ keV}$.

The proportion of photons P_h that reach altitudes between 0 and 30 km (y-axis), with an initial source set between 1 and 20 km of altitude (x-axis) and initial photon velocities directed upward, is shown on the left of Figure 23. The same results but with initial photon velocities directed downward, are shown on the right of Figure 23. Photons are more attenuated with downward velocities as the atmosphere is thicker at lower altitudes. In those simulations, we do not take into account bremsstrahlung from positrons (Dwyer, 2003) propagating back to the start of the avalanche. Positrons and the associated gamma rays produced by this bremsstrahlung are part of the RREA process and therefore it is worth mentioning that this phenomenon would probably enhance the detectability in the reverse direction when taken into account.

5.2. Detectability of Gamma Ray Glows

5.2.1. Using Kelley et al. (2015)'s Fluxes

In order to know in which conditions a gamma ray glow is detectable at 20 km of altitude, for instance for the next Stratéole-2 campaign (balloon flying at 20 km of altitude, see Section 2.3), we estimate the photon flux at different altitudes for a presumably strong gamma ray glow reported in the literature. We use the case reported by Kelley et al. (2015), who detected a glow-like event during the ADELE project and reported the measurement of the electron flux. They indeed estimated that the detector was in the electron source at the time of the event, with a measured flux of 1,100 electrons/cm²/s at 14.1 km of altitude (Kelley et al., 2015). This detection is believed to be done at the end of a downward RREA. In Appendix A, we show calculations and simulations using a toy

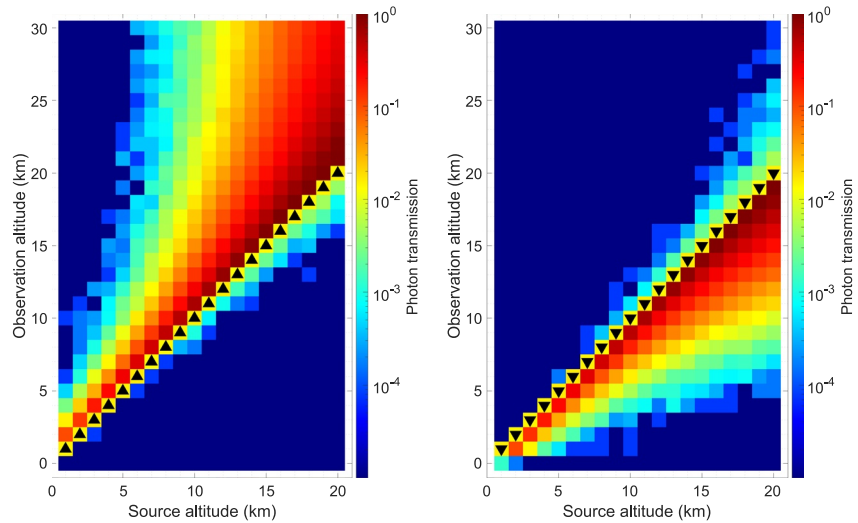


Figure 23. Proportion of photons P_h that reach a given altitude (or ratios of photon fluxes observed at various altitudes to fluxes at the source in the case of an infinite source plane). The source is set at different altitudes between 1 and 20 km, with initial photon velocities directed upward (left) and downward (right) (illustrated with black triangles).

model to determine the source gamma ray flux according to the electron flux measured by Kelley et al. (2015). We conclude that the gamma ray flux at the source (14.1 km) can be assumed to be ~ 340 photons/cm²/s. This gamma ray flux corresponds to ~ 48 times higher than the background at 14 km. The local flux calculated at different altitudes for different source altitudes is represented in Figure 24.

Using the flux deduced by Kelley et al. (2015) measurements and the estimations of P_h presented in Section 5.1, we estimate for which altitudes such a glow would have been detectable by XStorm, depending on the source altitude, using upward and downward initial velocities for photons. In this purpose, we use the background radiation

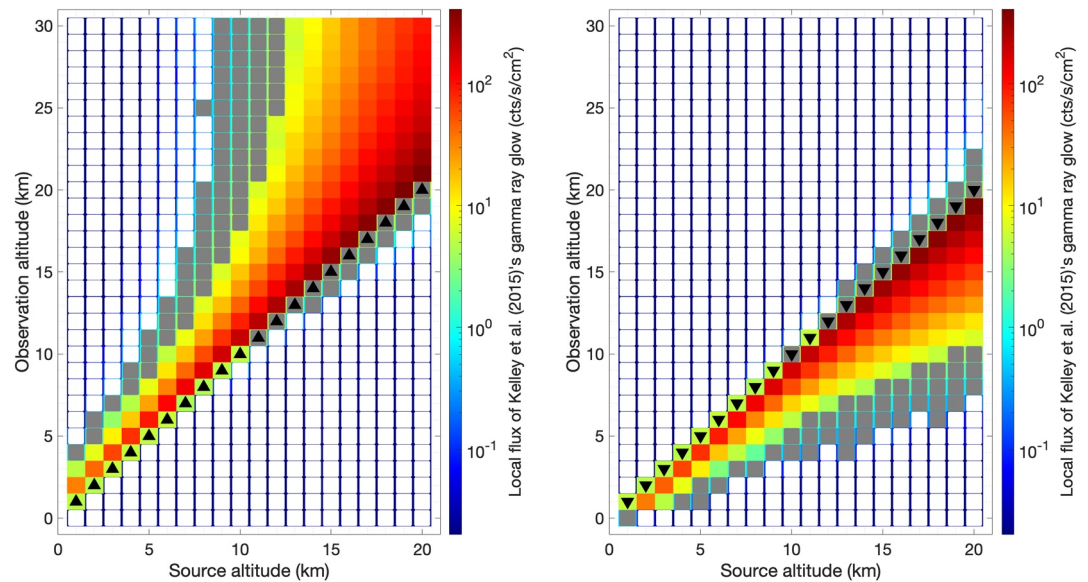


Figure 24. Estimation of local flux of the Kelley et al. (2015)'s gamma ray glow with upward (left) and downward (right) initial velocities for photons. The source is set at different altitudes between 1 and 20 km, with initial photon velocities directed upward (left) and downward (right) (illustrated with black triangles). Only the XStorm detectable glow configurations are filled, using the threshold calculation method presented in Section 3.4.2 and the background radiation level determined by both EXPACS between 0 and 20 km and fair weather balloon flight data at Aire-sur-l'Adour (France) (for altitudes greater than 20 km). The detection bin is set here as $\tau = 1$ s. The gray squares correspond to cases that are not detectable for a detection bin of 1 s, but would be detectable with a detection bin of $\tau = 60$ s.

level as a function of the altitude between 0 and 30 km of altitude, determined by the combination of EXPACS estimations (between 0 and 20 km) and balloon measurements with XStorm launched from Aire-sur-l'Adour (France) (used to obtain the radiation background at ground-level and to extrapolate EXPACS estimations above 20 km). The detectability of gamma ray glows with the method presented in Section 3.4.2 depends on the detection surface area of the detector. In fact, the threshold calculated is not proportional to the background radiation level but depends on the occurrence frequency of false positive events. For instance, using a detection bin of $\tau = 1$ s, for a background of 4 cts/cm²/s, the threshold is fixed at 7 cts/cm²/s, and for a background of 8 cts/cm²/s, the threshold will be fixed at 12 cts/cm²/s. This is due to the fact that Poisson likelihood does not increase linearly with the number of counts. Therefore, we determine the detectability of a glow using the geometric surface of XStorm, S_{XStorm} , that is a cube of 1" side, thus $S_{\text{XStorm}} = 6.45 \text{ cm}^2$.

The detectability by XStorm for a glow with a source flux of 340 photons/cm²/s depending on the source altitude and the initial photon velocity direction is plotted in Figure 24. According to Figure 23 (left), the flux at 20 km is equal to 7% of the flux at 14 km, and therefore would be equal to 24 photons/cm²/s. Such a glow would then be detectable, as the background radiation level at 20 km of altitude is ~ 8 photons/cm²/s (see Figure 17). Considering the same source, for photons propagating downward, we found that the flux at 20 km will be attenuated by 99.2% and will thus not be detectable by XStorm. More generally, using a detection bin of $\tau = 1$ s, XStorm on a Stratéole-2 balloon at 20 km will be able to detect upward gamma ray glows for sources between 10 and 20 km. Downward gamma ray glows will be detectable at 20 km only using a detection bin of $\tau = 60$ s for sources between 18 and 20 km of altitude.

The fact that for a source altitude of 1 km, a gamma ray glow is not detectable from the ground using a detection bin of $\tau = 1$ s (see Figure 24) is due to the significant natural radiation background of the ground directly estimated through XStorm measurements (note that EXPACS estimate only radiation level from cosmic rays).

It is worth mentioning that the reference glow chosen in those studies is a bright one reported by Kelley et al. (2015). Much fainter glows, likely more frequent, such as the one reported by Østgaard, Christian, et al. (2019), with a signal to noise ratio of about 1.4, require a longer triggering timescale than 1 s to be detected (this point is addressed in the next section). The triggering timescale is a variable parameter on XStorm, and a range of detection bins will be used simultaneously to optimize the detection of fainter glows for the next Stratéole-2 campaign. Moreover, they could still be detectable with the low-resolution data acquired every second. However, TGF single photon counts will be lost in the low-resolution data.

5.2.2. General Result: Minimum Detectable Source Flux

In order to give a more general result on the detection of gamma ray glows by XStorm, we have estimated the minimum detectable source flux (source gamma rays following a standard RREA spectrum, for photons with $E > 1$ MeV) as a function of the source altitude and the observation altitude. These estimations do not use Kelley et al. (2015)'s measurements. This estimation takes into account XStorm's surface and a detection time bin of 1 min. The lowest energy detectable by XStorm is assumed to be 400 keV. Results are shown in Figure 25. Results presented in Figure 24 can be deduced from this one.

5.3. XStorm Behavior for Østgaard, Christian, et al. (2019)'s 20-km Gamma Ray Glow

XStorm will be flying over balloon campaigns at 20 km of altitude for several months. We want to see if the high altitude gamma ray glow detected by Østgaard, Christian, et al. (2019) would have been detected by XStorm. For that, we used data from Østgaard, Christian, et al. (2019)'s (Figure 2E). We scaled the data using the proper detection surfaces of each detector. They used a detection surface of 3 BGOs of 15 cm \times 5 cm. We spread the time used, assuming that their aircraft fly at 250 m/s and that our balloon will fly at 5 m/s. The maximum of the glow should then be seen during ~ 8 min using a balloon instead of tens of seconds by aircraft (assuming that the gamma ray glow flux keeps constant over the flyby). Note that the sharp decrease after the main peak in Østgaard, Christian, et al. (2019)'s data has been shown to be associated with a rapid discharge process (Kochkin et al., 2021). The temporal and spatial components of such measurements are difficult to uncorrelate. We thus made the assumption that this decrease occurred within our minimum time bin, and would be observed on both balloon and aircraft the same way. A Poisson noise has been added to the data to be consistent with the size of the detector (using a random number generator following the Poisson distribution) and observations obtained during test flights.

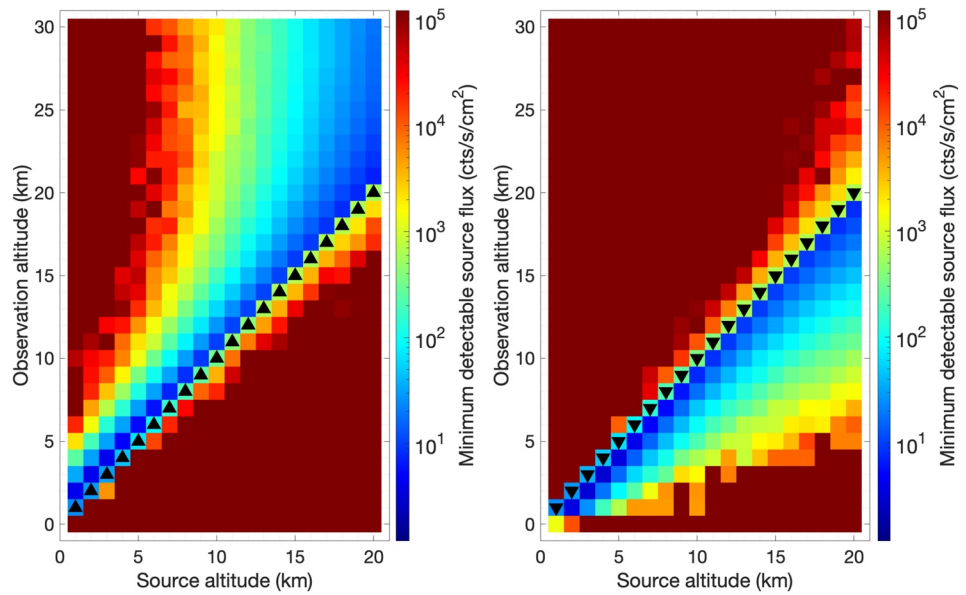


Figure 25. Minimum detectable source flux (cts/s/cm²) as a function of the source altitude and the observation altitude, for XStorm (surface detection of 6.5 cm²). The detection time bin has been fixed to 60 s. The triggering system is explained in Section 3.4.2.

Detection time bin of 1 s, 2 s, 10 s, 1 min, and 5 min have been used to know if the gamma ray glow would have been detected with XStorm. The triggering system used is the same as presented in Section 3.4.2 for gamma ray glows. The results can be seen in Figure 26. The light curve for each case has been divided by the detection time bin in order to plot all the data in one figure. One can see that the bin size of 1 s would detect the gamma ray glow. The faintest glow (around 400 min) would be detected using a time bin greater than 1 min.

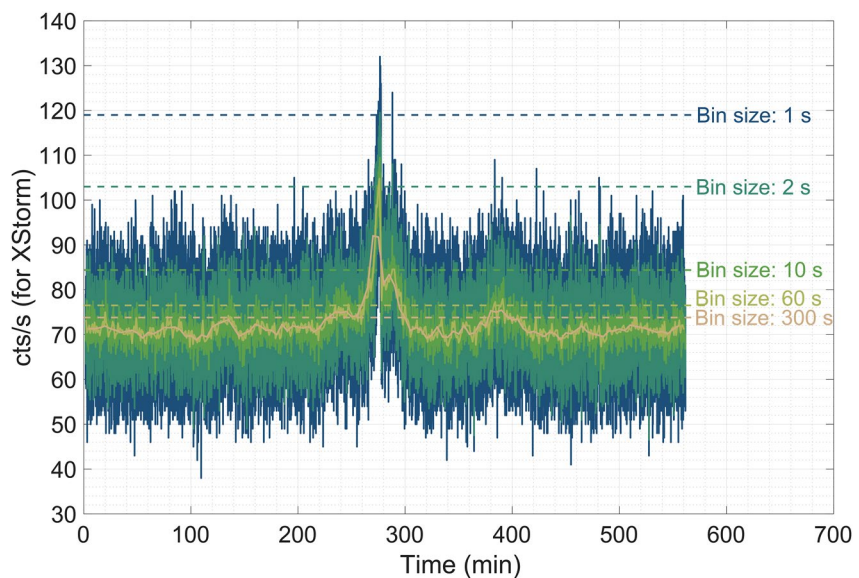


Figure 26. Data from Østgaard, Christian, et al. (2019)'s Figure 2E scaled to XStorm size, and to a balloon measurement (5 m/s velocity) instead of an airplane measurement (250 m/s velocity). The bin detection size is changed to see if the glow would be detected with bin up to 5 min. The dashed lines correspond to the detection threshold for each bin size used.

5.4. Probability to Detect a TGF

The detection of TGFs by balloon is believed to be less probable than gamma ray glows, because balloon flights are very close to the altitude of TGF sources. This proximity strongly limits the field of view of the detector. Stratéole-2 campaigns consist in balloons flying between 18 and 20 km of altitude for several-month durations. We hence expect a small but non-zero probability to detect such an event. To estimate the field of view of XStorm at 20 km of altitude for a 12-km TGF, we assume an upward TGF with an opening angle of 45° , photon directions isotropically distributed in the beam, a typical TGF source altitude of 12 km, and an observation performed at 20 km. 2,000,000 photons are used numerically, then scaled to 10^{18} photons assumed to be produced at the source. Monte Carlo simulations of photon fluxes show that at least 5 photons of the assumed TGF would be detected for radial distances smaller than ~ 20 km from the source, for XStorm detection area of ~ 6 cm². One can mention that this value is in good agreement with results presented in Hansen et al. (2013)'s Figure 5. We therefore assume that a TGF would be detectable within a 20 km-radius around the source. Using Fermi TGF catalog provided by Roberts et al. (2018), we calculate a map of TGF densities in units of/s/20 km-radius to take into account the field of view of XStorm, similarly to that shown in Pallu et al. (2023). Using the trajectories of the 8 balloon flights performed in the Stratéole-2 preliminary campaign in 2019 (with a mean of 85 days per flight), we calculate the probabilities to find one balloon in a TGF beam, applying the same method as described in Pallu et al. (2023). One finds that $\sim 1/2.3$ Stratéole-2 balloon flights will be able to detect a TGF. We will deliver four detectors to be flown on super-pressurized balloons for the next scientific campaign planned in 2025, thus we estimate the expected number of TGFs detected during the next campaign to be ~ 2 . Note that this value is an average and the true number of TGF detections might be significantly different.

6. Summary

XStorm is a newly developed lightweight gamma ray spectrometer, which aims to detect gamma ray glows and TGFs in close proximity. Several features are presented, for instance the ability to discriminate photons, neutrons, and electrons. First measurements in fair weather are shown, showing a nominal operation of the instrument at high-altitude, as well as the detection of the background radiation level as a function of the altitude, and the strategy adopted to avoid spurious TGF detections caused by instrumental effects. Finally, we have also shown calculations using Monte Carlo simulations to estimate the sensitivity of XStorm in the cited balloon campaigns to gamma ray glows and TGFs.

XStorm is designed to detect gamma ray glows and TGFs in close proximity. In the next months/years, participating to various measurements campaigns such as balloon campaigns and ground-based measurements presented here should bring new information in the field of high-energy atmospheric electricity. It could potentially detect the first TGF from balloon, providing a long duration high-energy context preceding the production of upward TGFs. It could detect other high altitude gamma ray glows, bringing valuable information on their nature and variety. It will also help us investigate the relation between gamma ray glows and TGFs.

Appendix A: Calculation of Fluxes From Kelley et al. (2015)'s Detected Gamma Ray Glow

We developed a toy model simulating the production of RREA in a 5-km side region with an exponential distribution that ends with a flux of $f_e = 1,100$ electrons/cm²/s at 14.1 km. The runaway electron density at the end of the avalanche at 14.1 km is:

$$n_e(14.1 \text{ km}) = \frac{f_e(14.1 \text{ km})}{v_e} = \frac{1,100/\text{cm}^2/\text{s}}{0.89c} = 0.0412 \text{ electron/m}^3 \quad (\text{A1})$$

where v_e is the mean electron velocity in a RREA (Coleman & Dwyer, 2006). We assume that the runaway electron density as a function of the altitude z is written as:

$$n_e(z) = n_0 \exp\left(-\frac{z}{\lambda}\right) \quad (\text{A2})$$

where n_0 is the initial runaway electron density and λ can be calculated from Equation 4 of Coleman and Dwyer (2006) and is dependent on the electric field amplitude. We use an electric field amplitude $E = 4$ kV cm⁻¹,

also used in simulations by Kelley et al. (2015), which gives $\lambda = 340$ m at 14.1 km. The density profile $n_e(z)$ is then fixed by the condition described in Equation A1. According to our simulation, the most part of the avalanche takes place within 3 km of altitude. This is also assessable using the avalanche multiplication factor estimated in Kelley et al. (2015) to be $\sim 4,500$. The number of avalanche lengths is then $\ln(4,500) \approx 8.4$, and thus the avalanche region is $8.4 \times \lambda \approx 2.8$ km long.

In the simulation, the position of each starting electron and each new electron injected to keep a steady state is randomly chosen following the exponential distribution of Equation A2. We propagate electrons and photons assuming their velocities to be respectively $v_e = 0.89c$ and c and directed upward, and we use a time step of $0.1 \mu\text{s}$ to calculate the new position of each particle. We fix the number of electrons in the simulation, and for each electron that reaches the limit altitude of 14.1 km, a new electron is injected following the exponential distribution of the positions. Then, we simulate the production of photons by each electron using the mean bremsstrahlung photon production (with energy >1 MeV) frequency ν_γ (e.g., Celestin et al., 2015) over the standard RREA spectrum, that is equal to $\sim 2.4 \times 10^5$ photon/electron/s. Photons are propagated without taking into account absorption explicitly (in the RREA and above) in the toy model. Figure A1 helps visualize the configuration of the simulated system. The position of electrons and photons, the distribution of the photon and electron fluxes in the simulation as a function of the altitude, and the flux at 14.1 km as a function of time are represented. The photon flux at 14.1 km is then found to be ~ 340 photons/cm²/s.

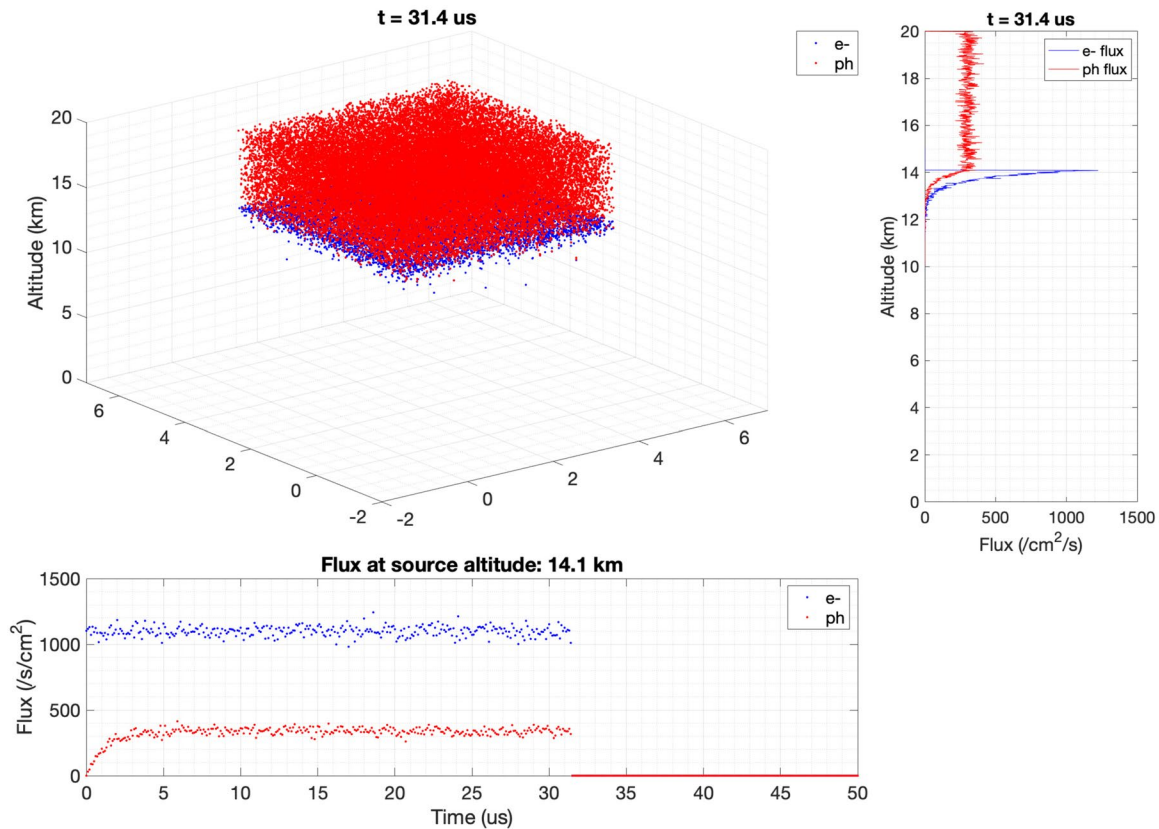


Figure A1. Simulation of a relativistic runaway electron avalanche with photon production in real time. The position of electrons and photons are plotted respectively in blue and red. The stationary photon flux at 14.1 km is reached within less than 5 μs . In this simulation, the photons do not undergo collisions, hence photon flux observed above 14.1 km is constant.

We compare this result with Kelley et al. (2015) measurements, using the gamma ray and electron spectra provided in their Figure 2. Integrating the spectra for energies >1 MeV, we obtain the ratio between the electron flux and the photon flux to be ~ 4.7 . Thus, we obtain a photon flux of 235 photons/cm²/s. This result is consistent

with our estimation, given that we used different physical parameters, in particular the cross-sections values to calculate ν_γ , and that in our case photons are not subjected to collisions.

Such result can be easily obtained analytically. Indeed, the differential equation driving the density of photons at 14.1 km (end of the RREA) as a function of the electron density can be written as:

$$\frac{\partial n_\gamma}{\partial t} + \vec{\nabla} \cdot (n_\gamma \vec{c}) = n_e \nu_\gamma \quad (\text{A3})$$

where n_γ and n_e are the photon and electron densities, \vec{c} is the speed of light, and ν_γ is the bremsstrahlung photon production frequency, $n_e \nu_\gamma$ represents the quantity of bremsstrahlung photons produced by the electrons per unit time. In steady state, $\vec{\nabla} \cdot (n_\gamma \vec{c}) = n_e \nu_\gamma$. Therefore, in one dimension it gives:

$$c \partial_z n_\gamma = n_e \nu_\gamma \quad (\text{A4})$$

Hence, using Equation A2:

$$n_\gamma(z) - n_\gamma(z_0) = \frac{\nu_\gamma}{c} \int_{z_0}^z n_e(z) dz = \frac{\nu_\gamma [n_e(z) - n_e(z_0)] \lambda}{c} \quad (\text{A5})$$

$n_e(z_0)$ is negligible and $n_\gamma(z_0) = 0$. We then obtain:

$$n_\gamma(z) = \frac{\nu_\gamma n_e(z) \lambda}{c} \quad (\text{A6})$$

With ν_γ and $\lambda \approx 340$ m calculated above, and $n_e(14.1 \text{ km})$ from Equation A1, we get $n_\gamma = 0.0153$ photons/m³, and therefore the photon flux at 14.1 km is:

$$f_\gamma(14.1 \text{ km}) = n_\gamma \times c = 334 \text{ photons/cm}^2/\text{s} \quad (\text{A7})$$

The model agrees well with the theoretical prediction.

The attenuation due to collisions can be taken into account in reducing the flux using the ratio determined in Section 5.1 for a source altitude of 14.1 km, as a function of the observation altitude using Monte Carlo modeling.

Data Availability Statement

The Fermi-GBM catalog is available online (at <https://fermi.gsfc.nasa.gov/ssc/data/access/gbm/tgff/>). The original data presented in this paper as figures may be downloaded from Pallu (2023).

References

- Abbasi, R. U., Abe, M., Abu-Zayyad, T., Allen, M., Anderson, R., Azuma, R., et al. (2017). The bursts of high energy events observed by the telescope array surface detector. *Physics Letters A*, 381(32), 2565–2572. <https://doi.org/10.1016/j.physleta.2017.06.022>
- Abbasi, R. U., Abu-Zayyad, T., Allen, M., Barcikowski, E., Belz, J. W., Bergman, D. R., et al. (2018). Gamma ray showers observed at ground level in coincidence with downward lightning leaders. *Journal of Geophysical Research: Atmospheres*, 123(13), 6864–6879. <https://doi.org/10.1029/2017JD027931>
- Adafruit (2023). adafruit.com. Retrieved from <https://www.adafruit.com/product/746>
- Belz, J. W., Krehbiel, P. R., Remington, J., Stanley, M. A., Abbasi, R. U., LeVon, R., et al. (2020). Observations of the origin of downward terrestrial gamma-ray flashes. *Journal of Geophysical Research: Atmospheres*, 125(23), e2019JD031940. <https://doi.org/10.1029/2019JD031940>
- Bertrand, G. H., Hamel, M., Normand, S., & Sguerra, F. (2015). Pulse shape discrimination between (fast or thermal) neutrons and gamma rays with plastic scintillators: State of the art. *Nuclear Instruments and Methods in Physics Research Section A: Accelerators, Spectrometers, Detectors and Associated Equipment*, 776, 114–128. <https://doi.org/10.1016/j.nima.2014.12.024>
- Bowers, G. S., Smith, D. M., Kelley, N. A., Martinez-McKinney, G. F., Cummer, S. A., Dwyer, J. R., et al. (2018). A terrestrial gamma-ray flash inside the eyewall of hurricane Patricia. *Journal of Geophysical Research*, 123(10), 4977–4987. <https://doi.org/10.1029/2017JD027771>
- Bowers, G. S., Smith, D. M., Martinez-McKinney, G. F., Kamogawa, M., Cummer, S. A., Dwyer, J. R., et al. (2017). Gamma ray signatures of neutrons from a terrestrial gamma ray flash. *Geophysical Research Letters*, 44(19), 10063–10070. <https://doi.org/10.1002/2017GL075071>
- Celestin, S., Xu, W., & Pasko, V. P. (2015). Variability in fluence and spectrum of high-energy photon bursts produced by lightning leaders. *Journal of Geophysical Research*, 120(12), 10712–10723. <https://doi.org/10.1002/2015JA021410>

Acknowledgments

This work is supported by the French space agency (CNES) in the framework of the projects OREO and STRATE-LEC, the French Institute of Radiation Protection and Nuclear Safety (IRSN), and Air France. We thank Drs. David Smith and Martino Marisaldi for useful discussions and Nikolai Ostgaard for the idea to perform high-energy calibration through the detection of muons. S.C. acknowledges support from the Institut Universitaire de France (IUF).

- Chilingarian, A., Daryan, A., Arakelyan, K., Hovhannisyanyan, A., Mailyan, B., Melkumyan, L., et al. (2010). Ground-based observations of thunderstorm-correlated fluxes of high-energy electrons, gamma rays, and neutrons. *Physics Reviews D*, 82(4), 043009. <https://doi.org/10.1103/PhysRevD.82.043009>
- Chilingarian, A., Mkrtchyan, H., Karapetyan, G., Chilingaryan, S., Sargsyan, B., & Arestakesyan, A. (2019). Catalog of 2017 thunderstorm ground enhancement (TGE) events observed on Aragats. *Scientific Reports*, 9(1), 6253. <https://doi.org/10.1038/s41598-019-42786-7>
- Cieślak, M. J., Gamage, K. A. A., & Glover, R. (2019). Critical review of scintillating crystals for neutron detection. *Crystals*, 9(9), 480. <https://doi.org/10.3390/cryst9090480>
- Coleman, L. M., & Dwyer, J. R. (2006). Propagation speed of runaway electron avalanches. *Geophysical Research Letters*, 33(11), L11810. <https://doi.org/10.1029/2006GL025863>
- Cummer, S. A., Lu, G., Briggs, M. S., Connaughton, V., Xiong, S., Fishman, G. J., & Dwyer, J. R. (2011). The lightning-TGF relationship on microsecond timescales. *Geophysical Research Letters*, 38(14), L14810. <https://doi.org/10.1029/2011GL048099>
- Cummer, S. A., Lyu, F., Briggs, M. S., Fitzpatrick, G., Roberts, O. J., & Dwyer, J. R. (2015). Lightning leader altitude progression in terrestrial gamma-ray flashes. *Geophysical Research Letters*, 42(18), 7792–7798. <https://doi.org/10.1002/2015GL065228>
- Dwyer, J. R. (2003). A fundamental limit on electric fields in air. *Geophysical Research Letters*, 30(20), 2055. <https://doi.org/10.1029/2003GL017781>
- Dwyer, J. R., Smith, D. M., & Cummer, S. A. (2012). High-energy atmospheric physics: Terrestrial gamma-ray flashes and related phenomena. *Space Science Reviews*, 173(1–4), 133–196. <https://doi.org/10.1007/s11214-012-9894-0>
- Dwyer, J. R., Smith, D. M., Uman, M. A., Saleh, Z., Grefenstette, B., Hazelton, B., & Rassoul, H. K. (2010). Estimation of the fluence of high-energy electron bursts produced by thunderclouds and the resulting radiation doses received in aircraft. *Journal of Geophysical Research*, 115(D9), D09206. <https://doi.org/10.1029/2009JD012039>
- Eack, K. B., Beasley, W. H., Rust, W. D., Marshall, T. C., & Stolzenburg, M. (1996). X-ray pulses observed above a mesoscale convective system. *Geophysical Research Letters*, 23(21), 2915–2918. <https://doi.org/10.1029/96GL02570>
- Eljen Technology (2023). eljentechnology.com. Retrieved from <https://eljentechnology.com/products/plastic-scintillators/ej-276>
- Enoto, T., Wada, Y., Furuta, Y., Nakazawa, K., Yuasa, T., Okuda, K., et al. (2017). Photonuclear reactions triggered by lightning discharge. *Nature*, 551(7681), 481–484. <https://doi.org/10.1038/nature24630>
- Fishman, G. J., Bhat, P. N., Mallozzi, R., Horack, J. M., Koshut, T., Kouveliotou, C., et al. (1994). Discovery of intense gamma-ray flashes of atmospheric origin. *Science*, 264(5163), 1313–1316. <https://doi.org/10.1126/science.264.5163.1313>
- Fishman, G. J., Briggs, M. S., Connaughton, V., Bhat, P. N., Paciesas, W. S., von Kienlin, A., et al. (2011). Temporal properties of the terrestrial gamma-ray flashes from the gamma-ray burst monitor on the Fermi observatory. *Journal of Geophysical Research*, 116(A7), A07304. <https://doi.org/10.1029/2010JA016084>
- Gironnet, J., Mikhailik, V., Kraus, H., de Marcellac, P., & Coron, N. (2008). Scintillation studies of Bi₄Ge₃O₁₂ (BGO) down to a temperature of 6 K. *Nuclear Instruments and Methods in Physics Research Section A: Accelerators, Spectrometers, Detectors and Associated Equipment*, 594(3), 358–361. <https://doi.org/10.1016/j.nima.2008.07.008>
- Groom, D. E., Mokhov, N. V., & Striganov, S. I. (2001). Muon stopping power and range tables 10 MeV–100 TeV. *Atomic Data and Nuclear Data Tables*, 78(2), 183–356. <https://doi.org/10.1006/adnd.2001.0861>
- Gurevich, A., Milikh, G., & Roussel-Dupre, R. (1992). Runaway electron mechanism of air breakdown and preconditioning during a thunderstorm. *Physics Letters A*, 165(5–6), 463–468. [https://doi.org/10.1016/0375-9601\(92\)90348-p](https://doi.org/10.1016/0375-9601(92)90348-p)
- Hansen, R. S., Østgaard, N., Gjesteland, T., & Carlson, B. (2013). How simulated fluence of photons from terrestrial gamma ray flashes at aircraft and balloon altitudes depends on initial parameters. *Journal of Geophysical Research: Space Physics*, 118(5), 2333–2339. <https://doi.org/10.1002/jgra.50143>
- Kelley, N., Smith, D., Dwyer, J., Splitt, M., Lazarus, S., Martinez-McKinney, F., et al. (2015). Relativistic electron avalanches as a thunderstorm discharge competing with lightning. *Nature Communications*, 6(1), 7845. <https://doi.org/10.1038/ncomms8845>
- Kochkin, P., Sarria, D., Lehtinen, N., Mezentsev, A., Yang, S., Genov, G., et al. (2021). A rapid gamma-ray glow flux reduction observed from 20 km altitude. *Journal of Geophysical Research: Atmospheres*, 126(9), e2020JD033467. <https://doi.org/10.1029/2020JD033467>
- Lu, G., Cummer, S. A., Li, J., Han, F., Smith, D. M., & Grefenstette, B. W. (2011). Characteristics of broadband lightning emissions associated with terrestrial gamma ray flashes. *Journal of Geophysical Research*, 116(A3), A03316. <https://doi.org/10.1029/2010JA016141>
- McCarthy, M., & Parks, G. K. (1985). Further observations of X-rays inside thunderstorms. *Geophysical Research Letters*, 12(6), 393–396. <https://doi.org/10.1029/GL012i006p00393>
- Østgaard, N., Christian, H. J., Grove, J. E., Sarria, D., Mezentsev, A., Kochkin, P., et al. (2019). Gamma ray glow observations at 20-km altitude. *Journal of Geophysical Research: Atmospheres*, 124(13), 7236–7254. <https://doi.org/10.1029/2019JD030312>
- Østgaard, N., Gjesteland, T., Stadsnes, J., Connell, P. H., & Carlson, B. (2008). Production altitude and time delays of the terrestrial gamma flashes: Revisiting the Burst and Transient Source Experiment spectra. *Journal of Geophysical Research*, 113(A2), A02307. <https://doi.org/10.1029/2007JA012618>
- Østgaard, N., Neubert, T., Reglero, V., Ullaland, K., Yang, S., Genov, G., et al. (2019). First 10 months of TGF observations by ASIM. *Journal of Geophysical Research*, 124(24), 14024–14036. <https://doi.org/10.1029/2019JD031214>
- Pallu, M. (2023). XStorm: A new gamma ray spectrometer for detection of close proximity gamma ray glows and TGF - FIGURES [figure]. [figshare. https://doi.org/10.6084/m9.figshare.23703942.v3](https://doi.org/10.6084/m9.figshare.23703942.v3)
- Pallu, M., Celestin, S., Trompier, F., & Klerlein, M. (2021). Estimation of radiation doses delivered by terrestrial gamma ray flashes within leader based production models. *Journal of Geophysical Research (Atmospheres)*, 126(8), e33907. <https://doi.org/10.1029/2020JD033907>
- Pallu, M., Celestin, S., Trompier, F., & Klerlein, M. (2023). Radiation risk assessment associated with terrestrial gamma ray flashes for commercial flights. *Journal of Geophysical Research: Atmospheres*, 128(6), e2022JD037569. <https://doi.org/10.1029/2022JD037569>
- Parks, G. K., Mauk, B. H., Spiger, R., & Chin, J. (1981). X-ray enhancements detected during thunderstorm and lightning activities. *Geophysical Research Letters*, 8(11), 1176–1179. <https://doi.org/10.1029/GL008i011p01176>
- Regener, E., & Pfozter, G. (1934). Intensity of the cosmic ultra-radiation in the stratosphere with the tube-counter. *Nature*, 134(3383), 325. <https://doi.org/10.1038/134325b0>
- Roberts, O. J., Fitzpatrick, G., Stanbro, M., McBreen, S., Briggs, M. S., Holzworth, R. H., et al. (2018). The first fermi-GBM terrestrial gamma ray flash catalog. *Journal of Geophysical Research: Space Physics*, 123(5), 4381–4401. <https://doi.org/10.1029/2017JA024837>
- Rutjes, C., Diniz, G., Ferreira, I. S., & Ebert, U. (2017). TGF afterglows: A new radiation mechanism from thunderstorms. *Geophysical Research Letters*, 44(20), 10702–10712. <https://doi.org/10.1002/2017GL075552>
- Sato, T. (2015). Analytical model for estimating terrestrial cosmic ray fluxes nearly anytime and anywhere in the world: Extension of PARMA/EXPACS. *PLoS One*, 10(12), 1–33. <https://doi.org/10.1371/journal.pone.0144679>
- Shao, X.-M., Hamlin, T., & Smith, D. M. (2010). A closer examination of terrestrial gamma-ray flash-related lightning processes. *Journal of Geophysical Research*, 115(9), A00E30. <https://doi.org/10.1029/2009JA014835>

- Smith, D. M., Bowers, G. S., Kamogawa, M., Wang, D., Ushio, T., Ortberg, J., et al. (2018). Characterizing upward lightning with and without a terrestrial gamma ray flash. *Journal of Geophysical Research: Atmospheres*, *123*(20), 11321–11332. <https://doi.org/10.1029/2018JD029105>
- Smith, D. M., Dwyer, J. R., Hazelton, B. J., Grefenstette, B. W., Martinez-McKinney, G. F. M., Zhang, Z. Y., et al. (2011). A terrestrial gamma ray flash observed from an aircraft. *Journal of Geophysical Research*, *116*(D20), D20124. <https://doi.org/10.1029/2011JD016252>
- Wada, Y., Enoto, T., Nakamura, Y., Furuta, Y., Yuasa, T., Nakazawa, K., et al. (2019). Gamma-ray glow preceding downward terrestrial gamma-ray flash. *Communications Physics*, *2*(1), 67. <https://doi.org/10.1038/s42005-019-0168-y>
- Workman, R. L. E. A., Burkert, V. D., Crede, V., Klempt, E., Thoma, U., Tiator, L., et al. (2022). Review of particle physics. *PTEP*, *2022*(8), 083C01. <https://doi.org/10.1093/ptep/ptac097>
- Zucchiatti, A., Bernini, C., Gervino, G., & Rottura, A. (1989). Temperature behaviour of a BGO prototype for use on a 4π high energy spectrometer. *Nuclear Instruments and Methods in Physics Research Section A: Accelerators, Spectrometers, Detectors and Associated Equipment*, *281*(2), 341–345. [https://doi.org/10.1016/0168-9002\(89\)91330-2](https://doi.org/10.1016/0168-9002(89)91330-2)